August 2015

Thermodynamic and Kinetic Simulation of Transient Liquid-Phase Bonding

Brad Allen Lindner
University of Wisconsin-Milwaukee

THERMODYNAMIC AND KINETIC SIMULATION OF TRANSIENT LIQUID-PHASE BONDING

by

Brad Lindner

A Thesis Submitted in

Partial Fulfillment of the

Requirements for the Degree of

Master of Science

in Engineering

at

The University of Wisconsin-Milwaukee

August 2015

ABSTRACT

THERMODYNAMIC AND KINETIC SIMULATION OF TRANSIENT LIQUID-PHASE BONDING

by

Brad Lindner

The University of Wisconsin-Milwaukee, 2015
Under the Supervision of Professor Benjamin C. Church

The use of numeric computational methods for the simulation of materials systems is becoming more prevalent and an understanding of these tools may soon be a necessity for Materials Engineers and Scientists. The applicability of numerical simulation methods to transient liquid-phase (TLP) bonding is evaluated using a type 316L/MBF-51 material system. The comparisons involve the calculation of bulk diffusivities, tracking of interface positions during dissolution, widening, and isothermal solidification stages, as well as comparison of elemental composition profiles. The simulations were performed with Thermo-Calc and DICTRA software packages and the experiments with differential scanning calorimetry (DSC), scanning electron microscopy (SEM), energy dispersive spectroscopy (EDS), and optical microscopic methods. Analytical methods are also discussed to enhance understanding. The results of the investigation show that while general agreement between simulations and experiments can be obtained, assumptions made with the simulation programs may cause difficulty in interpretation of the results unless the user has sufficient, mathematical, thermodynamic, kinetic, and simulation background.

For Jen, Maya, and Elliot

TABLE OF CONTENTS

LIST OF FIGURES

LIST OF TABLES

ACKNOWLEDGEMENTS

I wish to thank my advisor, Dr. Benjamin Church, for his assistance and the provision of experimental data.

I would also like to thank Steven Acker for calculation and summarization of much of the experimental data.

1. Introduction

Transient liquid-phase (TLP) bonding, also referred to as “diffusion brazing” in the context of braze systems, is a process in which a relatively low melting point material is used to create a metallurgical bond with the free surfaces of higher melting point materials. The low melting point or, “interlayer”, material is typically alloyed with one or more elemental melting point depressants that effectively reduce the liquidus temperature of a given composition range by facilitating the formation of a low melting point eutectic[1]. Because the stability of the low liquidus temperature relies on the presence of the melting point depressant (MPD), depletion of the MPD in the liquid (due to both diffusion of the liquid phase elements into the solid substrate material as well as diffusion of elements from the substrate into the liquid) causes the bond to solidify isothermally [2-4]. The MPD is chosen as an element that diffuses quickly, such as boron, and when full diffusion occurs, a uniform bond is produced at a relatively low temperature [4, 5]. This homogenization due to diffusion is responsible for a major advantage of diffusion brazing, which is that the resulting bond has a higher melting point than that of the initial interlayer material and in some situations may approach that of the substrate material [6].

Diffusion brazing is not without its challenges; however, as the complete isothermal solidification and homogenization necessary to create a seamless joint can take a

significant amount of time. The exact length of time for complete diffusion depends on the alloy system and processing variables, and includes: temperature, interlayer metal thickness (also referred to as joint gap and clearance), the presence of impurities, the formation of intermetallic phases, and the mutual solubility of the materials [1, 7-10]. The application of TLP bonding to manufacturing processes, therefore, requires an understanding of the complex and interrelated variables presented by both the alloy systems and processing.

The basis for a streamlined and accurate approach to understanding and predicting many of these variables lies in the understanding and efficient application of thermodynamic and kinetic principles.

In this investigation, the use of numerical simulation software is applied to the heterogeneous phase equilibria and diffusion behavior of a Type 316L austenitic stainless steel substrate and a AWS BNi-5b nickel-based (Metglas® MBF-51) foil interlayer. The results obtained are compared to those obtained experimentally. Type 316L was chosen due to its wide usage in applications requiring improved sensitization resistance. MBF-51 was also chosen due to popularity in brazing of stainless steels and superalloys.

1.1 Objective

Many industries determine the viability of new materials, processes, and parameters by production sampling “trial and error” techniques. Typically a baseline is established - which is either the current properties of a component or process, historical precedence, or educated hypotheses - and samples are run that are in some way different from this baseline. Testing of the new or revised product is performed for characterization and comparison to the baseline. In the manufacturing or processing of materials this testing usually involves microscopic evaluation, chemical analyses, and various mechanical tests. Due to the considerable time and cost associated with sample runs (and the inevitable iterative re-runs), any methods that can reliably minimize or eliminate certain aspects of this process are valuable tools. The purpose of this investigation is to evaluate thermodynamic and kinetic numerical simulation software as an enhancement to or possibly a replacement for the traditional trial and error techniques still used for planning, prediction, and sampling of new components, materials, and processes [11].

1.2 Scope of Present Study

This investigation is concerned with the overall applicability of numerical simulation software to the metallurgical systems and processes, therefore, only a very general aspect of the often nuanced and complex science behind TLP bonding is treated.

In the following investigation, the author has knowingly omitted considerations of surface cleanliness of the faying surfaces, surface reactions, the effects of pressure while brazing, the formation of porosity, surface energy effects, wetting phenomena, fluid dynamics, and curvature of the interfaces. Although grain boundary diffusion plays a significant role in some cases [12], it is not treated in this investigation. Two (2) stages of the TLP process are considered in this investigation: dissolution and isothermal solidification.

2. Background

2.1 Overview of the 316L / MBF-51 System

In the current investigation, the substrate material is Type 316L austenitic stainless steel and the interlayer is MBF-51 (AWS BNi-5b) amorphous brazing foil; the compositions of which are detailed in Table 2.1.

Table 2.1 *– Chemical Composition (in wt%) of the Substrate/Interlayer Materials*

Element	Type 316L Base Material, Actual	BNi-5 (MBF-51) Braze Foil, Actual
Carbon	0.02	<0.001
Manganese	1.44	0.01
Silicon	0.58	7.42
Phosphorus	0.03	<0.005
Sulfur	0.04	<0.005
Chromium	16.07	13.62
Nickel	10.02	Remainder
Molybdenum	2.00	<0.005
Copper	0.47	<0.005
Vanadium	0.07	<0.005
Cobalt	0.11	0.05
Boron	<0.001	1.23
Iron	Remainder	0.58

Type 316L stainless steel contains is generally used in applications that require additional resistance to sensitization upon exposure to elevated temperatures. At room temperature, the microstructure is fully austenitic.

MBF-51 is a nickel-based alloy designed specifically for brazing applications with a reported melting range of 1030 to 1126˚C and containing two (2) melting point depressants: boron and silicon [13]. Because boron is an interstitial element, it has a higher diffusivity than silicon, which is a substitutional element. Despite the differences in diffusivities, depression of the melting point and isothermal solidification in this alloy requires the interrelated effects of both boron and silicon and, therefore, MBF-51 is best represented as a ternary system.

2.1.2 Intermediate Phases

Boron is a critical the melting point depressant that facilitates isothermal solidification in many braze interlayer alloys; however, due to low solubility in nickel, it can also form brittle intermediate compounds, usually with chromium, that degrade both the mechanical properties and corrosion resistance of the joint[5, 8], as illustrated in Figure 2.1.

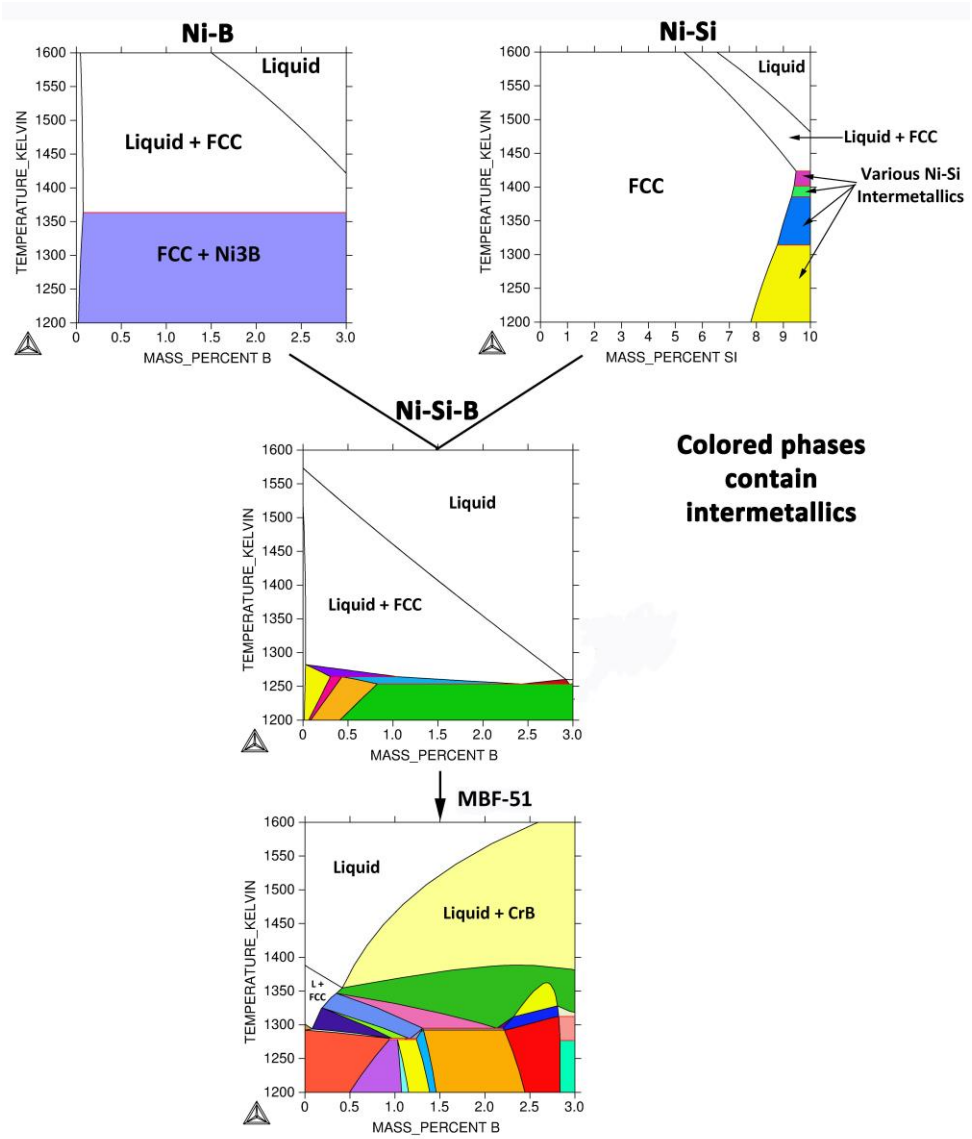

Figure 2.1- Illustration of possible intermediate phases that may form during solidification of MBF-51.

If a seamless joint free of intermediate boride phases is required, either full isothermal solidification must be completed or a homogenization treatment must be performed. If isothermal solidification is interrupted by cooling, a dendritic cast structure with the attendant solute rejection (i.e. coring) will result [3]. Note that silicon can also form intermediate phases but its solubility is much greater in both nickel and iron.

Lugscheider, et al, has previously evaluated type 316L stainless steel with a Ni-based interlayer. [7, 8]; however, the experiments performed only report the outcomes caused by variation of physical variables, such as foil thickness, isothermal hold temperature, and time, and have very little discussion of relations to thermodynamic and kinetic variables. Researchers have studied other types of austenitic stainless steels with Ni-based interlayers; namely Arafin [14] (Type 321-BNi-2) and Chen [15] (Type 304-BNi-2).

2.2 Process Steps in Transient Liquid-Phase Bonding

To ensure a sound braze joint in as short amount of time as possible, the interlayer material must be mutually soluble with the substrate material [10, 16]. Once an appropriate interlayer composition is chosen, deposition of the interlayer material between the substrate faying surfaces is due either to direct placement of the braze material on the faying surface(s) or indirectly via capillary mechanisms. After the interlayer material is in place, the system is heated above the liquidus of the interlayer material but below the liquidus of the substrate material. The liquid interlayer material then flows into all regions of the joint by capillary action [10, 17]. The entire braze system is held at an elevated temperature (which is not always the initial braze temperature) for a suitable amount of time to facilitate diffusion of the MPD and subsequent isothermal solidification.

To conceptualize TLP bonding, the process is generally presented as four (4) discrete stages: heating, dissolution and widening, isothermal solidification, and homogenization, as illustrated in Figures 2.2 and 2.3. Binary eutectic systems are commonly used in the literature for illustrative purposes [2-4, 17-20]; however, note that this is often done primarily for ease of interpretation and does not indicate that TLP bonding requires a simple eutectic system. In this investigation, the formalism developed by Macdonald and Eagar[2] and later modified by Zhou, et al. [18] is used, namely:

Stage 1 - Heating

The system is heated from a low temperature (usually room temperature) to the solidus temperature of the interlayer material. Solid-state diffusion dominates this stage and occurs to an extent dependent on the material systems involved and process variables, such as surface conditions, interlayer thickness, heating rate, and pressure. Because solid-state diffusion is relatively slow and the heating stage occurs fairly rapidly, the diffusion is typically assumed to be minimal. Many researchers argue that even if there is non-trivial diffusion during this stage that it would be immediately re-dissolved into the liquid during the dissolution stage, causing the MPD species to go back into solution and negate any prior diffusion [2, 3, 18, 21].

Stage 2a – Dissolution

When the temperature of the system surpasses the interlayer solidus temperature, base metal dissolution begins due to diffusion of the MPD depressant from the liquid interlayer into the solid substrate. The need to maintain a mass balance at the solid/liquid interface (assuming a closed system) causes dissolution of the substrate material [6]. Dissolution typically occurs very quickly because it only involves short-range diffusion and the total time required may be only a few seconds [2-4, 18, 22].

Stage 2b – Widening of the Liquid Phase

Like dissolution, widening occurs due to the need to maintain a mass balance - the diffusion of the substrate species into the interlayer liquid occurs much more rapidly than the diffusion of the liquid species into the solid substrate. Widening continues because the concentration of the MPD depressant element(s) in the substrate at the interface exceeds the stable liquidus concentration of the substrate material [2-4, 18]. The liquid phase attains maximum width (commonly referred to as “maximum gap width”) when the liquid attains thermodynamic equilibrium with the substrate material and becomes homogenous. The time required to achieve the maximum gap width is a function of the diffusion rates for various species and the interlayer thickness.

Stage 3 – Isothermal Solidification

Once the maximum gap width is achieved, which corresponds to saturation of the liquid with base metal constituents, the liquid is assumed homogenous and the composition

remains at the liquidus composition of the equilibrium phase diagram at the isothermal hold temperature. As solute diffuses out of the liquid, mass balance is maintained by shrinking of the liquid width via isothermal solidification. This stage is controlled by long-range solid-state diffusion of the melting point depressant into the substrate material (i.e. MPD crosses the interface from liquid to solid) and accordingly, can take a relatively long time. When the final solidification occurs, a solute peak with the solidus composition will be present at the center line [21, 23].

Stage 4 - Homogenization

Homogenization is similar to an annealing or normalizing heat treatment. After isothermal solidification, there is still a peak of interlayer composition at the center of the joint. The goal of homogenization is to eliminate this chemical inhomogeneity at the interface via solid-state diffusion. Because solid-state diffusion is the dominant process, this stage can take quite long.

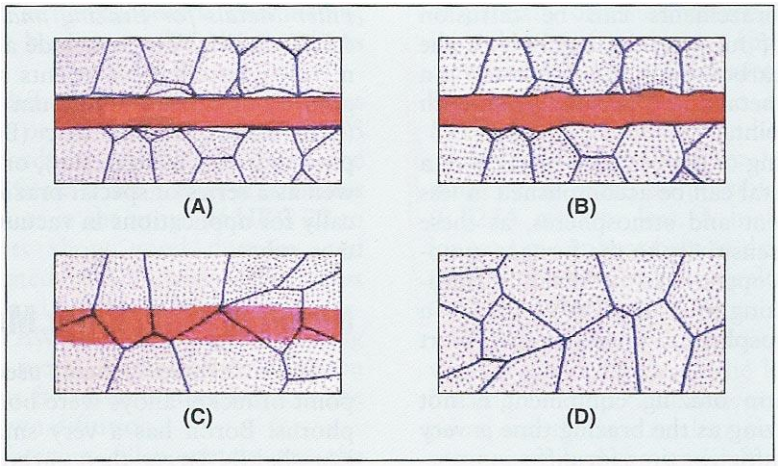

Figure 2.2- The stages of TLP bonding are (A) heating, (B) dissolution and widening, (C) isothermal solidification, and (D) homogenization. Figure taken from reference [10].

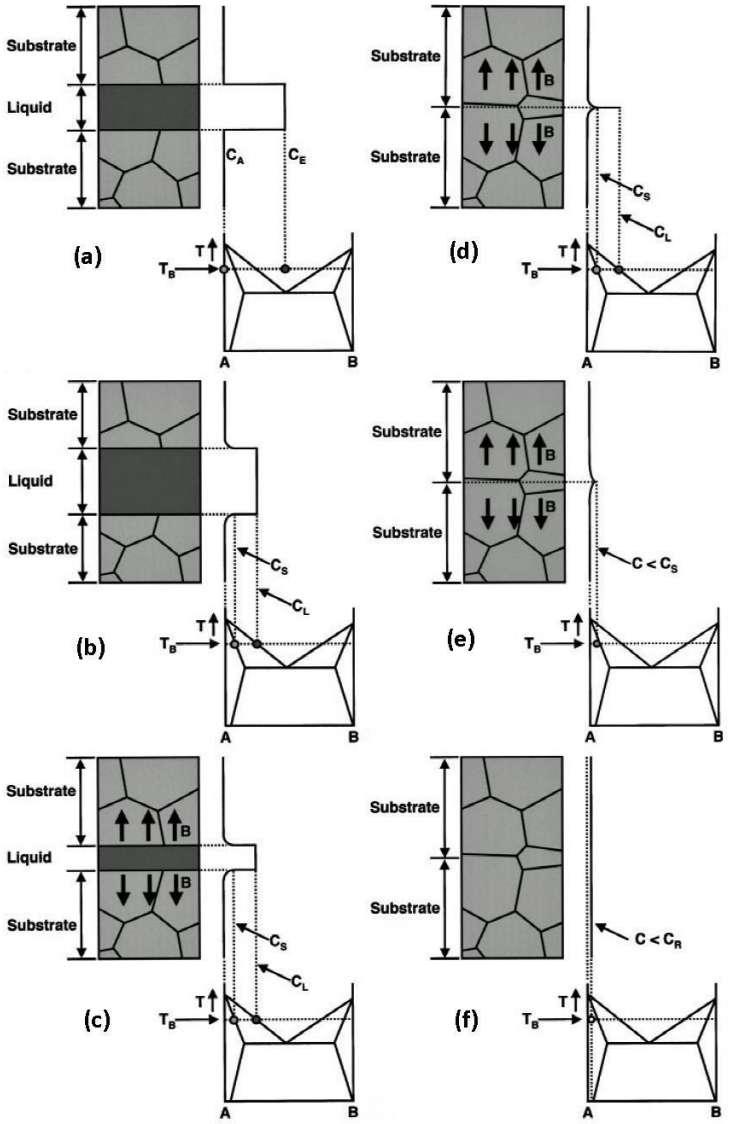

Figure 2.3- The stages of TLP bonding are shown with the coinciding concentration profiles and the hypothetical binary phase diagram: (a) represents the initial dissolution, (b) is widening of the liquid, (c) and (d) are isothermal solidification, (e) is homogenization, and (f) is the final "seamless" condition. Image taken from reference [22].

As previously noted, the time required to complete each stage is dependent on material and geometric variables. Cook and Sorensen [6] proposed a simplification to conceptualize the process times - starting with Stage 2, each stage takes about an order of magnitude longer than the stage preceding it.

There is general agreement among researchers that, while the composition of the bulk liquid remains homogeneous (at the liquidus concentration of the binary phase diagram), determination of the equilibrium concentrations at the interlayer/substrate interface are difficult to accurately determine during isothermal solidification because realistically, the liquid composition is not constant. The consideration of a ternary system also complicates evaluation. For an isobaric and isothermal binary system there are zero degrees of freedom, but for a ternary there is one. The implication is that instead of having an invariant point, there is a range of liquid compositions and multiple localized equilibrium constants shifting throughout isothermal solidification, as illustrated in Figure 2.4. In this scenario, a shifting tie-line approach is required to account for the constantly changing composition of the liquid phase as discussed in papers by Sinclair [23, 24], Boettinger [25-27], and Kuntz [28].

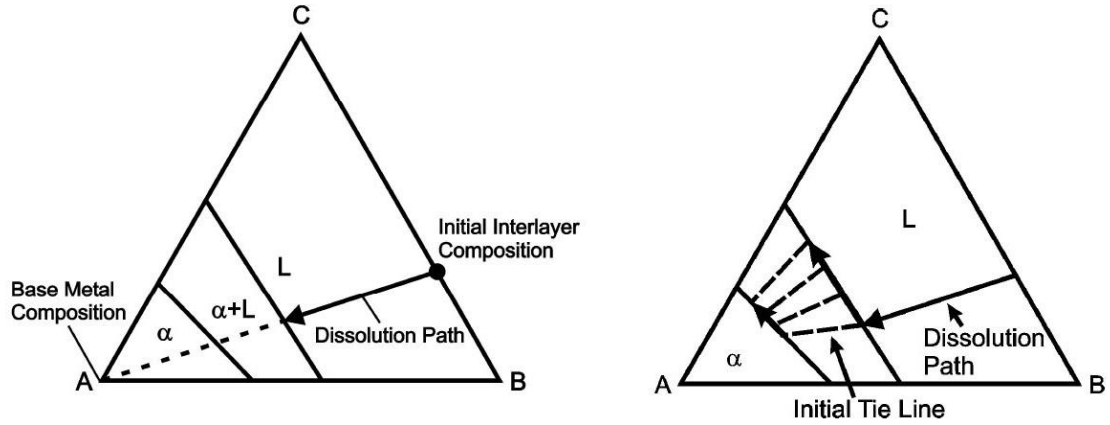

Figure 2.4- The shifting tie-line approach for ternary systems is illustrated. Ideally, dissolution occurs on a straight line from the initial interlayer composition to the base metal composition (left); however, compositional dependence requires a shifting tie-line approach (right). Image taken from [3].

The extra degree of freedom in a ternary system allows the forcing of a single interface velocity for both solutes. The solute with the larger rate constant (i.e. higher interface velocity) will define the interface movement.

2.3 Prediction of TLP Bonding Kinetics

2.3.1 Analytical Methods Background

2.3.1.1 Kinetics

Numerous analytical methods have been used to predict TLP bonding kinetics; most use variations of the Nernst equation for substrate dissolution and Fick's laws for isothermal solidification. Although many researchers use slightly different forms of the same general equations due to their particular boundary conditions, most of the analytical models have the following assumptions attached [12, 29]:

- The system is one-dimensional unless grain boundary diffusion is considered, which requires a two-dimensional model.
- There are no initial barriers to interaction of the filler metal with the substrate such as surface reactions or oxides.
- Both the interlayer material and substrate are initially homogenous and, in binary systems, the liquid phase remains homogenous throughout the process.
- The interlayer and substrate materials maintain thermodynamic equilibrium at the interface during the entire process.
- Fick's equations apply; specifically, moving boundary solutions using a semi-infinite substrate and thin film interlayer.
- Movement of the interface is planar, which ensures a constant interface area.
- Mass conservation is maintained at all times.

Dissolution and Widening

Analytical solutions to model the dynamic heating from the interlayer melting point to the braze temperature are extremely difficult to perform and, therefore, the assumption is made that time required for heating is very small or that dissolution starts when the braze temperature is achieved [18]. For base metal dissolution in relatively simple systems, variations of the Nernst-Brunner equation are commonly used, which assume a bulk liquid zone with a thin boundary film at the solid liquid interface [2, 18, 29-31]:

$$C_L = C_{sat}\left[1 - \exp\left(-K\left(\frac{A}{V}\right)\right)t\right] \quad \text{(Equation 1)}$$

where C_L is the solute concentration in the liquid, C_{sat} is the solute concentration at saturation, V is the solution volume, A is the reaction surface area, and K is a rate constant for dissolution. C_{sat} is determined by slope of liquidus line at the appropriate location in the phase diagram and K is determined with the Arrhenius equation. Note that if this treatment is used to describe a multi-phase system, the equation must be applied separately to each phase in the system. Zhang and Shi [32] solved the Nernst equation in terms of solubility and diffusion coefficients:

$$W_t = \left(\frac{\rho_{interlayer}}{\rho_{substrate}}\right) \cdot \gamma_L \cdot W_i \cdot \left[1 - \exp\left(-\frac{\alpha \cdot t}{W_i}\right)\right] \quad \text{(Equation 2)}$$

where W_t is the initial width of the interlayer, ρ is density, t is time, and γ and α are the solubility and dissolution coefficients, respectively, which are determined experimentally.

The Nernst-Brunner approach has significant problems due to the assumptions of a finite substrate and a bulk liquid (the interlayer); specifically, calculations result in liquid and interface widths of the same order of magnitude. This is not an accurate

representation of a real system and, furthermore, results in a system with no boundaries such that dissolution occurs past the size of a finite system.

Methods based on error function operations have also been presented, but these assume a binary eutectic interlayer and only apply from the solidus to the liquidus temperature of the interlayer material (i.e. the two-phase region). In this case, dissolution can only be predicted *before* the interlayer material fully transforms to liquid.

The conclusion among most researchers is that analytical methods for prediction of the dissolution of the substrate have significant flaws due to the restrictive boundary conditions required for solution. Numerical simulation methods are required to accurately characterize this aspect of TLP bonding.

Isothermal Solidification

In contrast to the attempted analytical description of substrate dissolution, there is good agreement between the experimental results and analytical models used to describe the isothermal solidification stage. Because isothermal solidification is solid-state diffusion controlled, all of the analytical models are based on solutions to Fick's laws. In the applications of these laws to binary systems the liquid is assumed homogenous during isothermal solidification and, therefore, solute diffusion in the liquid can be ignored [18].

For a one-dimensional system, Fick's 1st law defines the mass flux as a function of a concentration gradient on line "x".

$$\mathrm{J} = -\mathrm{D}\left(\frac{\partial \mathrm{C}}{\partial \mathrm{x}}\right) \quad \text{(Equation 3)}$$

where *J* is the mass flux, *D* is the diffusion coefficient, *C* is the concentration of the solute, and *x* defines the flux direction.

Fick's 2nd law in one-dimension assuming *D* is *independent* of position, concentration, and time is:

$$\left(\frac{\partial \mathrm{C}}{\partial \mathrm{t}}\right) = \mathrm{D}\frac{\partial^2 \mathrm{C}}{\partial \mathrm{x}^2} \quad \text{(Equation 4)}$$

Fick's 2nd law assumes mass is conserved and the mass balance is defined as:

$$(\mathrm{C_L} - \mathrm{C_S})\frac{\mathrm{d}}{\mathrm{dx}}\mathrm{X(t)} = \mathrm{D_S}\frac{\partial}{\partial \mathrm{x}}\mathrm{C_S} - \mathrm{D_L}\frac{\partial}{\partial \mathrm{x}}\mathrm{C_L} \quad \text{(Equation 5)}$$

where C_L and C_S are the liquidus and solidus concentrations of the solute, respectively, at the solid/liquid interface, *X(t)* is the position of the interface, and D_S and D_L are the solute diffusivities in the solid and liquid, respectively [33].

Fick's second law becomes practically useful only when clearly defined boundary conditions are applied and the differential equation is solved. As previously noted, all of the discussed solutions assume equilibrium at the solid/liquid interface, which means that the solidus composition is defined by an isothermal tie line on the appropriate equilibrium phase diagram [3]. Using these boundary conditions, the solution to Fick's 2nd law is:

$$C(x,t) = C_S + (C_O - C_S) \cdot \mathrm{erf}\left(\frac{x}{2\sqrt{Dt}}\right) \qquad \text{(Equation 6)}$$

Forms of this equation have been used with the assumption of a stationary interface, shifting reference frame solutions, and moving boundary (i.e. interface) solutions. For TLP bonding, the moving boundary model is regularly used due to its relative accuracy when compared to experimental results. Applying the moving boundary assumptions to Equation 6, the final form is used to determine the total time required to complete isothermal solidification:

$$t_s = \frac{W_{max}^2}{16(D)(K^2)} \qquad \text{(Equation 7)}$$

where W_{max} is the maximum gap width, t_s is the time required to complete isothermal solidification, and K is an interface rate parameter. Note that t=0 at the beginning of the isothermal solidification step (i.e. maximum gap width of the joint).

All of the analytical procedures reviewed in this investigation require determination of solute concentrations at various points on a phase diagram; however, if the studied system is not a binary or simple ternary, significant complications arise. To deal with the heterogeneous equilibria of complex systems, the calculation of phase diagrams is required.

2.3.1.2 Thermodynamics

Combination of the first and second laws of thermodynamics and the application of various constraints yields the basic equation for Gibbs energy:

$$\mathrm{G} = \mathrm{H} - \mathrm{TS} \qquad \text{(Equation 8)}$$

where *H* is enthalpy, *T* is temperature, and *S* is entropy.

When solving analytically, Equation 8 is typically used in the context of an ideal or regular solution model. Because understanding of the numerical methods used in the current investigation are aided by a brief overview of phase diagram calculations, the basic steps for finding the Gibbs energy of an arbitrary phase, identified as "γ", is

discussed in the context of a regular solution model. The Gibbs Energy of the example phase is defined as [34]:

$$G^{\gamma} = G^{0}_{ref} + G^{ideal}_{mix} + G^{excess}_{mix} \quad \text{(Equation 9)}$$

with the free energy terms defined as:

$$G^{0}_{ref} = x_A G^{0}_{A} + x_B G^{0}_{B} + \cdots x_i G^{0}_{i} \quad \text{(Equation 10)}$$

This represents the total free energy of the system *before* the components are mixed. G_A^0 and G_B^0 are the molar Gibbs energies of pure A and B at the reference temperature and pressure. Assuming an ideal solution model (i.e. *ΔH=0*) and applying the Boltzmann Equation, configurational entropy, and Stirling's approximation gives the total free energy of the system *after* mixing of the components [35, 36]:

$$\Delta G^{\gamma}_{mix(ideal)} = RT[x_a \ln(x_a) + x_b \ln(x_b) + \cdots x_i \ln(x_i)] = -T\Delta S$$

(Equation 11)

Because the regular solution model is used, however, $\Delta H \neq 0$ and the energy due to bonding conditions must be considered:

$$\Delta H_{mix}^{\gamma} = \Omega(\mathrm{x_a x_b} \cdots \mathrm{x_i}) \quad \text{(Equation 12)}$$

where *x* is the mole fraction of an element in the phase and *Ω* is the interaction parameter. The Gibbs Energy expression for the regular solution model is therefore

$$\Delta G_{mix}^{\gamma} = \Omega(\mathrm{x_a x_b} \cdots \mathrm{x_i}) + \mathrm{RT}[\mathrm{x_a ln(x_a)} + \mathrm{x_b ln(x_b)} + \cdots \mathrm{x_i ln(x_i)}] \quad \text{(Equation 13)}$$

Given the relationship between Gibbs Energy and chemical potential,

$$\mu_{\mathrm{i}} = \left(\frac{\partial \mathrm{G}}{\partial \mathrm{n_i}}\right)_{T,P} \quad \text{(Equation 14)}$$

the expression for a regular solution may be written,

$$\mu_{\mathrm{i}} = \mathrm{G_i} + \Omega(1 - \mathrm{x_i})^2 + \mathrm{RTln(x_i)} \quad \text{(Equation 15)}$$

The application of this method at a given temperature, as well as finding common tangent points on the Gibbs Energy - Composition curves (to ensure phase stability), and transferring these points to temperature-composition space, is how phase diagrams are constructed. Many iterations of this method at different temperatures will provide more points that can be connected and eventually form the phase boundaries. The properties of different phases within the same system are independent of one another;

i.e. changes in one phase do not necessarily affect other phases and, therefore, all of the phases in a multicomponent heterogeneous system must have their own expressions for Gibbs Energy. Because the phase with the lowest Gibbs Energy in the system will be the most stable, the equilibrium state at a discrete temperature (and constant pressure) can be predicted with the condition that the chemical potential (μ) must be equivalent in all phases [37].

The Gibbs energy expressions alone do not give enough information to easily create a phase diagram and so Gibbs Phase Rule (Equation 16) is necessary.

$$f = \mathrm{C} - \mathrm{P} + 2 \qquad \text{(Equation 16)}$$

where *f* is the degrees of freedom, *C* is the number of system components, and *P* is the number of stable phases.

2.3.2 Numerical Simulation Background

From the preceding discussion, it is apparent that a significant amount of time and effort are required to create a phase diagram, even when using relatively simple systems and basic thermodynamic models. Additionally, the assumptions of the regular solution model (and most other basic models), while good approximations, are often too simplistic to accurately represent complex heterogeneous equilibria.

Numerical simulation of diffusion processes involves finite difference methods that provide approximate solutions by converting complex differential equations into a discrete set of smaller problems with a finite number of degrees of freedom. Generally, simulation of the TLP bonding process is performed by iteratively solving the previously discussed thermodynamic and kinetic equations. A primary advantage of this is that the TLP bonding process is treated as a series of sequential steps and not as the separate, discrete stages of the analytical treatments.

Both thermodynamic and kinetic models are needed not only for accurate representation of real systems, but also as concurrent tools in problem solution. For example, if the interface in a system (such as a solid-liquid moving boundary in a diffusion couple) is considered as the separation between two (2) phases, the principles of phase equilibria can be applied locally to model what is happening at the interface.

2.3.2.1 Thermodynamics

Thermodynamic databases are the backbone of phase diagram prediction and kinetic simulation in material systems. The databases are created using experimental data and by extrapolation using the CALPHAD (CALculation of PHase Diagrams) approach, as illustrated in Figure 2.5.

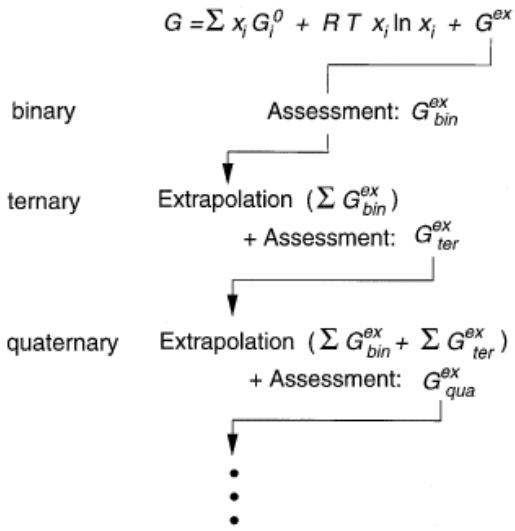

Figure 2.5- The CALPHAD approaches uses known data from lower order systems to predict the behavior of higher order systems [38].

The derived thermodynamic expressions are used to solve the Gibbs energy equations for all the phases in the system of interest and find the conditions for global energy minimization. The calculation is defined so that the degrees of freedom are minimized enough to allow calculation of an initial Gibbs energy and these estimates are functions of the phases present. Iterative numerical techniques (i.e. finite difference) are then used until the change in Gibbs energy between subsequent calculations is small enough to approximate series convergence - this convergence is taken as the minimized Gibbs energy [35].

2.3.2.2 Kinetics

For multicomponent diffusion with a moving interface, Fick's 2nd law is still used but the diffusion coefficients are contained in a matrix and must be solved numerically in order to model the concentration profile as a function of time. The displacement of the phase boundary is due to the flux [39]. Fick's first law is used in matrix form to solve the diffusion equation for an n-component system [40, 41].

$$-J_i = \sum_{j}^{n-1} D_{ij} \frac{\partial c_j}{\partial_x} \qquad \text{(Equation 17)}$$

where J_k is the flux of species k, D_{kj}^{n} is the matrix of diffusivities, and $\frac{\partial c_j}{\partial_z}$ is the concentration gradient. This matrix form of this equation facilitates the effects of interrelated elements; i.e. that the concentration gradient of an element may causes another element to diffuse [42]. Recall that the diffusion equation used for analytical solutions assumes a constant diffusion coefficient. If the diffusivity is not constant but varies as a function of concentration, Equation 4 has no simple analytical solutions and numerical methods are required to solve the more general form:

$$\left(\frac{\partial C}{\partial t}\right) = \left(\frac{\partial}{\partial x}\right)\left(D\frac{\partial C}{\partial x}\right) \qquad \text{(Equation 18)}$$

Additionally, extension to ternary and higher order systems requires the introduction of additional variables into Fick's laws to account for the additional components. This results in a series of linear partial differential equations that must be solved simultaneously.

$$\frac{\partial C_i}{\partial t} = \sum_{k=1}^{n-1} \frac{\partial D_{ik}}{\partial x} \left(\frac{\partial C_j}{\partial X} \right) \qquad \text{(Equation 19)}$$

The rate of a diffusion controlled phase transformation is determined not only by the diffusivities of the species in the system but also by the mobility of the interface. Because interface movement is assumed to be thermally activated, the mobility is modeled using an Arrhenius expression and the dependence of the local composition on these mobilities is determined by the extrapolation of experimental data from lower-order systems [43].

2.3.3 Prior Work Using Numerical Methods

Many researchers have reported on the use of numerical simulation methods. In 1991, Nakagawa, et al. [29] used an explicit finite difference method that iterated Fick's 2nd Law coupled with a mass balance to simulate a step-wise advance of the interface during TLP bonding of Ni using an Ni-P interlayer. Local equilibrium at each step was found by iteration of partition coefficients in the Ni-P binary system and assumptions of both infinite and finite heating rates from the eutectic temperature to the hold

temperature. The findings for the infinite heating rate were that the total dissolution time is proportional to the square root of the interlayer thickness (the filler metal thickness is a significant variable) and the interface velocity approximately relates to the inverse square root of the MPD diffusivity in the liquid – meaning that movement of the interface is diffusion dependent. For finite heating rates, it was concluded that for thin interlayers, lower heating rates caused less substrate dissolution at any given temperature and negligible dissolution at the brazing temperature. This method was also used on a similar alloy system by Ikeuchi, et al. [12] but with the inclusion of grain boundary diffusion, which required the solution of two-dimensional non-steady state diffusion problems. Ikeuchi found that faster isothermal solidification rates that more closely approximated the experimental results were more dependent on liquid penetration at the grain boundaries, which changes the solid-liquid interfacial area, and consideration of the interfacial energy due to curvature of the solid-liquid interface, than by increased MPD diffusivity at the grain boundaries.

Zhou, et al. [18] used a semi-implicit finite difference method that allowed simulation in a continuous rather than step-wise manner. Zhou also concluded that, while the prediction of dissolution requires numerical simulation, isothermal solidification can be predicted by using analytical methods if grain boundary diffusion is neglected. Illingworth, et al. [44] derived a fully implicit using a system of coupled non-linear equations, eliminating the step-size limitation inherent in explicit methods. Later evaluation of the moving phase boundary model by Illingworth, et al. [45] led to the

conclusion that, in some cases, substitutional elements may allow faster TLP solidification than interstitial elements due to their higher solubilities in the substrate material.

Sinclair [23] modeled isothermal solidification in a ternary system assuming linear phase boundaries, a Zener (i.e. linear) diffusion profile in the solid, and a negligible diffusion profile in the liquid and concluded that isothermal solidification in higher order systems occurs initially by a shifting tie-line governed by coupled mass balances, indicating that the composition of the liquid is not homogenous as assumed in a binary system, but changes continuously [43]. Campbell and Boettinger [43] modeled the ternary Ni-Al-B system and found good correlation with experimental results for both the position of interface and solid-phase composition profiles. The composition profiles in the liquid phase, however, did not show good agreement and it was hypothesized that this was caused by the concentration dependence of the mobilities.

In general, most researchers report good correlation with experimental results; however, the conclusions tend to be alloy system specific and the formation of intermediate phases complicates interpretation.

2.4 Experimental Characterization of TLP Bonding

The most common methods of performing the diffusion brazing processes for experimental characterizations are with wedge shape joint gap specimens [5, 7, 15, 16,

32] or “sandwich” diffusion couples that are furnace-brazed in vacuum or inert atmosphere [4, 8, 19, 46, 47]. More recently, differential scanning calorimetry (DSC) has been increasingly used with “half” samples (only one interface) [3, 21, 28, 33, 48]. Regardless of the method used to complete the brazing operations, the brazements all have subsequent testing performed and may include mechanical, microstructural, and/or chemical characterizations. Often, these results are compared to the previously discussed analytical and numerical solutions with the primary goal of more accurate future predictions.

Only the characterization methods used in the current investigation will be discussed: differential scanning calorimetry (DSC), microstructural examination, and scanning electron microscopy (SEM) / energy dispersive spectroscopy (EDS).

2.4.1 Microstructural Methods

Microstructural (metallographic) methods rely on optical measurement of the remaining interlayer and diffusion zone thicknesses to determine the position of the interface at various isothermal hold times. Tuah-Poku, et al. [4] assumed that, upon solidification due to cooling, all of the remaining liquid transforms to a eutectic phase and, therefore, metallographic measurement of the average eutectic phase thickness (area of eutectic phase in a photomicrograph divided by length) is equivalent to the thickness of the liquid layer immediately prior to cooling. Macdonald and Eagar [2, 49] point out that this method neglects the solidification that occurs between the isothermal hold

temperature and the eutectic temperature. Because there is no easy way to visually resolve non-eutectic solidification due to cooling, they derived a lever rule approach that provides the total solidified thickness or width (pre-eutectic + eutectic):

$$\mathrm{f_L} = \frac{\mathrm{C_L} - \mathrm{C_S}}{\mathrm{C_E} - \mathrm{C_S}} \qquad \text{(Equation 20)}$$

where C_E is the composition of the eutectic, C_S is the solidus composition, C_L is the liquidus composition, and f_L is the eutectic (i.e. optically measured) fraction of the total amount solidified. The total amount solidified is then:

$$\mathrm{W_T} = \mathrm{W_{Measured}} + (1 - \mathrm{f_L})\mathrm{W_{Measured}} \qquad \text{(Equation 21)}$$

where the optically measure eutectic width is $W_{Measured}$ and the total width is W_T. This method is considered a good approximation as long as the assumption of equilibrium solidification is accurate.

Metallography is also used to obtain quantitative fractions of various dispersed phases.

2.4.2 Scanning Electron Microscopy and Energy Dispersive Spectroscopy

Scanning electron microscopy (SEM) and Energy Dispersive Spectroscopy (EDS) are useful tools to confirm the features observed during metallographic examination and

are often used to characterize the diffusion composition profiles in addition to chemical identification of dispersed phases. EDS composition profiles have been shown by multiple researchers to correspond to the predicted concentration profiles determined numerical simulation [27, 41, 49].

In the current investigation, SEM is also used to measure the eutectic zone thickness using the metallographic techniques presented in Section 2.4.1.

2.4.3 Differential Scanning Calorimetry

DSC was previously noted as one of the ways the brazing procedure is completed; however, it also actively characterizes thermal events of the braze cycle.

DSC methods have been successfully applied to a number of binary braze systems: Ag-Cu [3, 33, 48], Ni-BNi2 [20], and wrought aluminum alloys [21] and are often compared with analytical solutions, chemical analysis, microscopy, and/or numerical simulations. Furthermore, the DSC is used to determine diffusion coefficients via cooling curve methods.

Kuntz, et.al [3, 28, 33, 48] in particular has done much research using DSC, in which the liquid remaining after various isothermal hold periods is measured by comparing the endothermic and exothermic events during melting and solidification, respectively. These experiments all found that the percent remaining liquid decreased linearly with

the square root of isothermal hold time. These experiments also found that the fraction of remaining liquid is time dependent – thicker layers take longer to complete melting and dissolution. This means that when comparing the effect of different interlayer thicknesses, consideration should be given to the different dissolution rates. Ruiz-Vargas, et. al. found that the fraction of dissolved base metal was proportional to the initial thickness of the interlayer [20].

3. Experimental Procedures

3.1 Sample Preparation

In the ongoing experiments performed at the University of Wisconsin – Milwaukee, differential scanning calorimetry (DSC) is used to complete and measure the brazing process. The experimental methods used for the experiments discussed in the current investigation are summarized by as follows [50]:

Preparation of Substrate

The substrate material is Type 316L stainless steel in rod form (5mm diameter), which was cut into approximately 2mm thick "pucks" that are mounted in bakelite, ground and final polished with 1 micron alumina suspension. The polished samples are broken out of the mounts, re-cleaned, and coated with alumina on all but the polished (faying) surface which acts as a braze stop-off.

Preparation of Interlayer

The form of the BNi-5 braze interlayer is 38 micron thick MBF-51 foil. Circular pieces of the braze foil are punched out of the foil to match the rod diameter and cleaned ultrasonically in isopropyl alcohol followed by rinsing in acetone. The foil is then weighed and the initial mass is recorded.

3.2 Brazing Procedures

The braze foil is placed in an alumina crucible and the polished surface of the Type 316L puck is placed on top of the braze foil. This 316L substrate/BNi-5 foil couple is then loaded into a Netzsch STA 449-F1 thermal analysis system (i.e. DSC) along with an identically prepared Type 316L puck (but no BNi-5 foil) to be used as a reference. Once 316L/BNi-5 braze system and the reference 316L puck are loaded into the furnace chamber, the atmosphere is prepared by multiple flushes with high purity argon gas and once the atmosphere is acceptably inert, the brazing cycle(s) can be performed.

Braze Cycles

Two (2) brazing experiments are discussed in this investigation to highlight different aspects of the characterization process:

1. The samples are heated to brazing temperatures of 1323K (1050˚C), 1373K (1100˚C), and 1423K (1150˚C) and held for 360, 3600, and 18000 seconds at each temperature, followed by cooling to room temperature. This data collected by the DSC was used to track the change in interface position and solve for the diffusion coefficient.
2. One (1) sample was heated to a brazing temperature of 1523K (1250˚C) and held for five (5) minutes, followed by cooling to 873K (600˚C) and holding isothermally for five (5) minutes before heating back up to the brazing temperature for a total of three cycles (i.e. 15 minutes total at 1523K). After the

third hold at 1523K, the sample is cooled to room temperature. This data from this experiment was used to characterize the diffusion of elements as a function of distance from the original substrate/foil interface; i.e. the composition profiles.

The heating and cooling rate of the samples for both experiments was 20K/min.

3.3 Characterization Techniques

3.3.1 Differential Scanning Calorimetry

When the braze system is heated past the liquidus temperature of the foil, an endothermic occurs due to the additional energy required for melting. Conversely, when the melt solidifies, the heat of fusion released creates an exothermic event. The energy absorbed or released during these events is highly dependent on alloy composition. Calculating the area under the curves; i.e. the integral of the DSC curves, gives the enthalpy (H) for an event and a typical example is shown in Figure 3.1. During dissolution of the interlayer and subsequent isothermal solidification, the composition of the liquid changes as well as the transition temperatures and enthalpies. If the system is cooled so that the interlayer solidifies and is then re-heated, the enthalpy of melting will be different than it was previously due to these compositional changes. Additionally, the smaller the area is under a given curve, the less energy was released during solidification, which corresponds to less material solidified. Therefore, the area under the curve is an indirect measurement of how much liquid transformed to solid.

Because the foil is the only material that melts in the system, the amount of liquid at any given time is assumed equivalent to the amount of foil remaining. This is essentially how the DSC is able to indirectly measure changes in position of the interface.

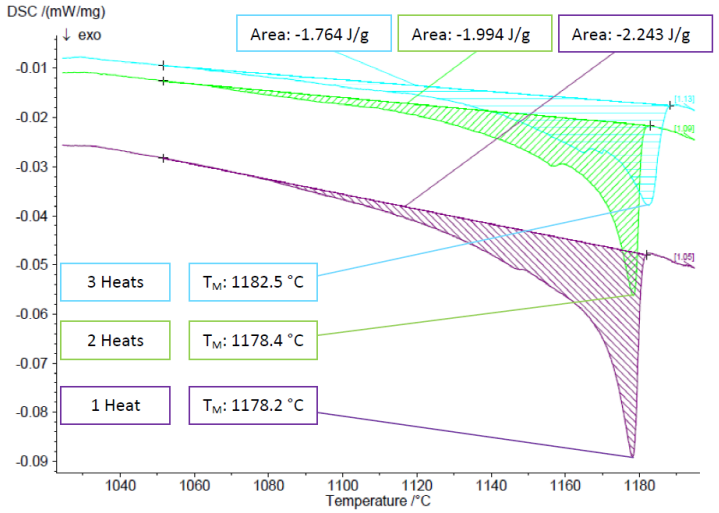

Figure 3.1- The DSC curves for brazing cycle number 2 are shown. The shading represents the area under the endothermic peaks, which is the enthalpy (H).

A commonly used empirical equation [3] is used to relate the area under the curve to the actual amount of braze material solidified:

$$W_{liquid} = \frac{\Delta H_{measured}}{\Delta H_{fully\ eutectic}} \qquad \text{(Equation 21)}$$

The difference between the original amount of braze material (the measured mass of the foil before insertion into the crucible) and the remaining amount (area under curve and equation 20) is allows determination of the amount of liquid remaining or, conversely, the amount of foil that has undergone enough of a compositional change to

solidify isothermally. Using standard relationships, the amount of foil that has isothermally solidified is converted to volume and then to the height; i.e. thickness, of the isothermally solidified zone. The original thickness of the foil (which is also the original or “Matano”) interface position is subtracted from the thickness of “pure” BNi-5 remaining after processing to yield the thickness of the isothermally solidified zone. The thicknesses of the isothermally solidified layers of three (3) different temperatures and times are then used to determine the diffusion coefficients and diffusion equation from the system.

3.3.2 Scanning Electron Microscopy and Energy Dispersive Spectroscopy

The samples brazed for 5, 10, and 15 minutes (300, 600, and 900 seconds; respectively) at 1523K were analyzed using a scanning electron microscope (SEM) equipped with an Energy Dispersive Spectrometer (EDS) having two detection modes. In the standard mode, elements from atomic number 11 (sodium) and above on the Periodic Table can be detected with a minimum detection limit of approximately 0.1 to 0.2 weight percent. The resulting spectrum may then be quantified and the results are normalized to 100%. The primary elements that are not detected by standard EDS analysis, and are excluded from normalization, are carbon and oxygen. These are detectable by "light element" mode EDS analysis. However, light element EDS spectra cannot be consistently and reliably quantified and the minimum detection limits for carbon and oxygen are relatively high. Due to these characteristics, EDS is considered a "semi-quantitative" analysis.

In this investigation SEM and EDS were primarily used to obtain experimental concentration profiles of silicon, chromium, iron, and nickel. Boron is a “light” element and was therefore unable to be quantified.

4. Experimental Results

In the sections that follow, discussion of the results will use the standard DICTRA coordinate system, which starts all measurements from the left system boundary, as illustrated in Figure 4.1.

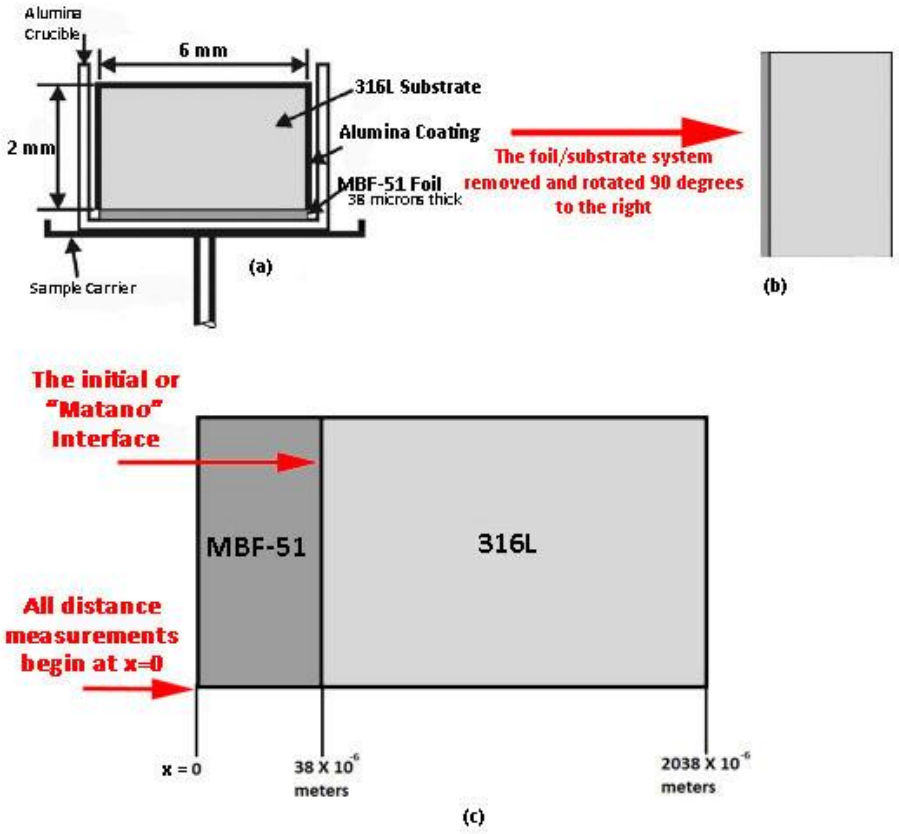

Figure 4.1– (a) The DSC system is orientated as shown. (b) To visualize the simulation in Dictra, imagine that the foil/substrate system is removed and flipped on its side. (c) The system shown in (b) after enlarging and annotating to illustrate how distances are measured in the Dictra. Images (a) and (b) were adapted from Kuntz, et.al [28].

4.1 Determination of Diffusion Coefficients

The DSC results of braze cycle #1 (samples heated to brazing temperatures of 1323K (1050˚C), 1373K (1100˚C), and 1423K (1150˚C) and held for 360, 3600, and 18000 seconds at each temperature) are detailed in Table 4.1 - note that the MBF-51 foil is referred to as “liquid”. This is done both to keep consistency with terms used in the reviewed technical literature and also to reinforce that the liquid remaining after isothermal solidification is not “pure” foil, but a (typically) eutectic alloy that may have a similar composition to MBF-51 but, due to dissolution of the substrate and other diffusional effects, is not anticipated to be “pure” MBF-51 foil.

***Table 4.1**- DSC Results for Braze Cycle No. 1*

1323K Primary Phase						
Time, seconds	Time^1/2, seconds	H (system), J/g	H (foil), J/g	Initial Foil Amount, mg	Final Liquid Amount, mg	Liquid Remaining, %
360	18.97	80.79	207	5.40	2.11	39.03
3600	60.00	73.63	207	5.20	1.85	35.57
18000	134.16	54.50	207	5.20	1.37	26.33
1373K Primary Phase						
Time, seconds	Time^1/2, seconds	H (system), J/g	H (foil), J/g	Initial Foil Amount, mg	Final Liquid Amount, mg	Liquid Remaining, %
360	18.97	79.13	207	5.40	2.06	38.23
3600	60.00	67.46	207	5.40	1.76	32.59
18000	134.16	38.42	207	5.40	1.00	18.56
1423K Primary Phase						
Time, seconds	Time^1/2, seconds	H (system), J/g	H (foil), J/g	Initial Foil Amount, mg	Final Liquid amount, mg	Liquid Remaining, %
360	18.97	84.93	207	5.10	2.09	41.03
3600	60.00	65.31	207	5.10	1.61	31.55
18000	134.16	25.73	207	5.90	0.73	12.43

Assuming a cylindrical geometry and using standard relationships, the amount of liquid that has isothermally solidified is converted to volume and then to height, which corresponds to the relative change in position of the MBF-51/316L interface. The liquid composition is expected to be similar to MBF-51 and, therefore, the calculations use the density of MBF-51 as reported by Metglas, Inc. (7.73 g/cm^3) [13]. Because isothermal solidification occurs due to diffusion mechanisms, this height can be related to the amount of gross diffusion into and out of the liquid. The distances (i.e. heights of the isothermally solidified cylindrical volume elements) for the three (3) different hold temperatures and times were then plotted against the square root of time ($x \propto \sqrt{Dt}$) and fitted with linear regression lines, as shown in Figure 4.2. The slope of the regression lines are the square roots of the diffusion coefficients ($\sqrt{D}$).

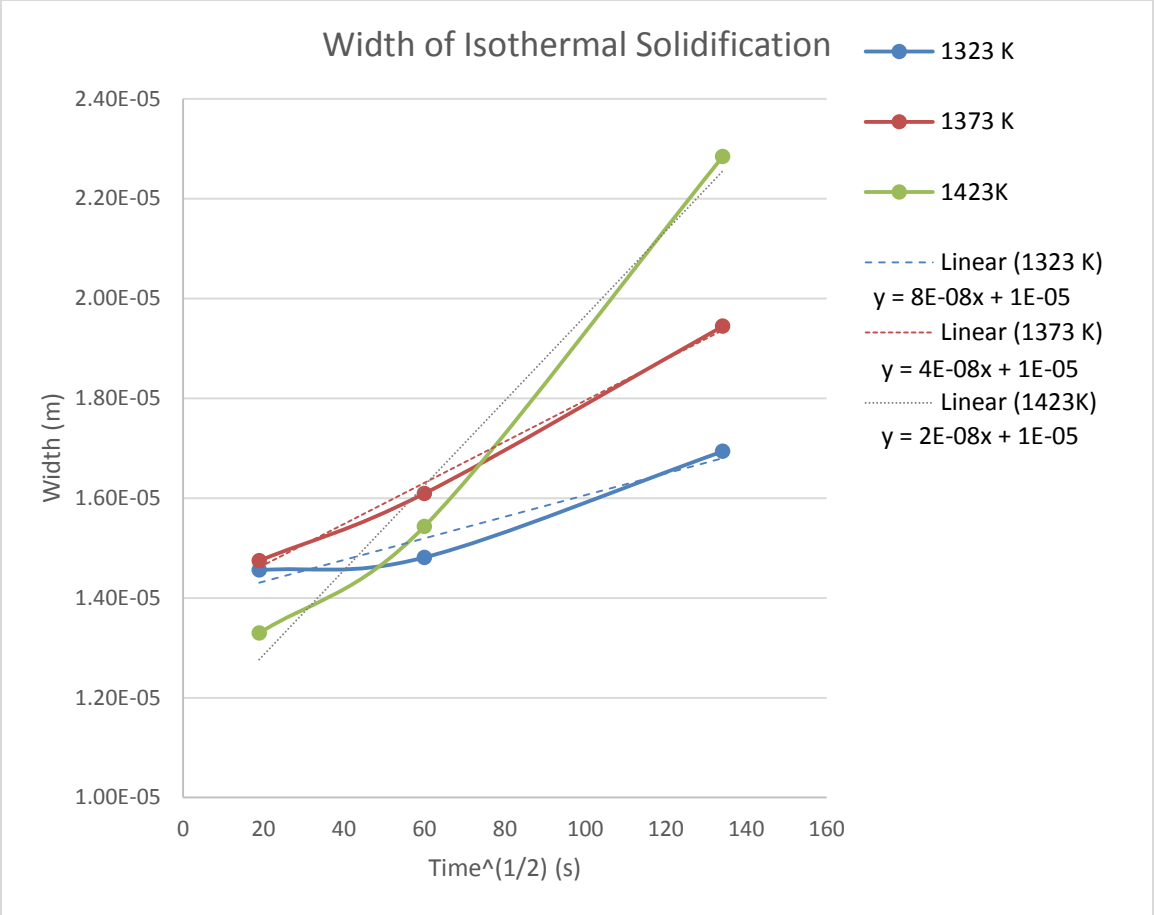

Figure 4.2- The width of the isothermally solidified zone is plotted against the square root of time. The slopes of the linear regression lines are the square root of the approximate bulk diffusion coefficients at a given hold temperature.

The experimental diffusion coefficients for the 1323, 1373, and 1423 (K) temperatures are 6.4 X 10^{-15}, 1.6 X 10^{-15}, and 4.0 X 10^{-16} m^2/s; respectively.

The pre-exponential (D_o) and the activation energy required for diffusion to occur (Q_d) were solved by using the Arrhenius form equation of a first-order integrated rate law [51, 52].

$$D = D_o exp\left(-\frac{Q_d}{RT}\right)$$ (Equation 22)

where R is the universal gas constant, and T is the temperature in Kelvin. In the form of a straight line:

$$\ln(D^2) = \ln(D_o) - \left(\frac{Q_d}{R}\right)\left(\frac{1}{T}\right)$$ (Equation 23)

$$y = b + (m)(x)$$

Therefore, plotting ln(*D*) versus T^{-1} allows empirical determination of the pre-exponential (y-intercept) and activation energy (slope) or, from the graph shown in Figure 4.3.

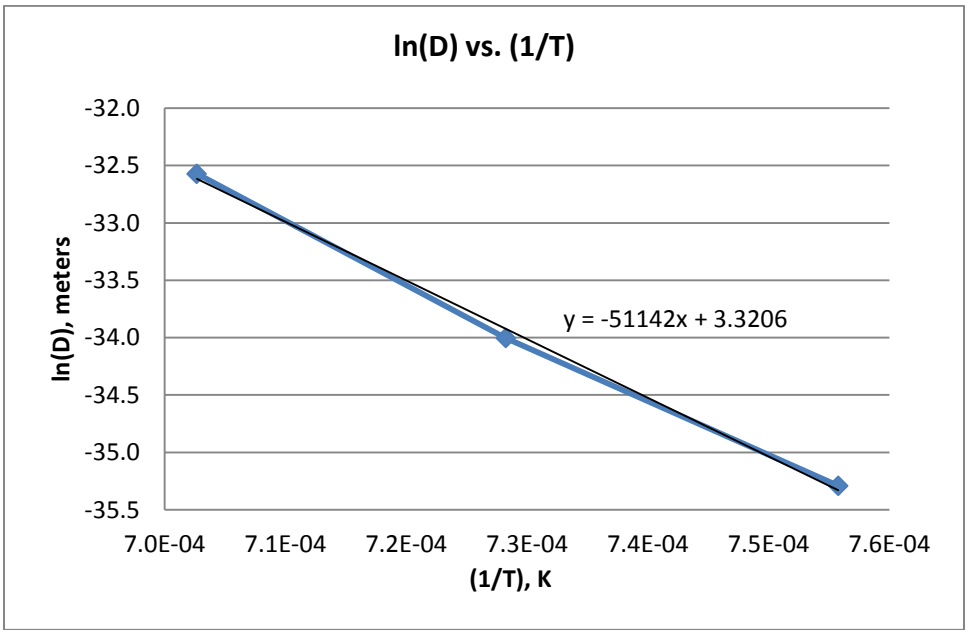

Figure 4.3- The plot of ln(*D*) versus T^{-1}. The pre-exponential term is the y-intercept and the activation energy is the slope.

4.2 Determination of Interface Positions

The position of interface (POI) after brazing was determined with three (3) different methods:

Method 1

The POI of the sample held at 1423K (braze cycle #1) after 60, 3600, and 18000 seconds was estimated by converting the remaining liquid % DSC output to distance, and is summarized in Table 4.2.

Table 4.2**- Summary of Estimated Interface Positions – **Isothermal Hold at 1423K

Time, seconds	Position of Interface, microns
360	13.77
3600	10.61
18000	4.81

Method 2

The POI of the sample held at 1523K (braze cycle #2) after 300, 600, and 900 seconds, as shown in Figures 4.4 through 4.9, was estimated with the metallographic methods discussed in Section 2.4.1. This was first determined by assuming that all of the remaining liquid solidified from a eutectic composition (neglecting any solidification that occurred on cooling from the hold temperature to the eutectic). Using the coordinate system discussed previously, the thickness of the non-isothermally solidified zone is equivalent to the interface position. Next, Equations 19 and 20 were used with the appropriate compositions from the Ni-B binary phase diagram. The results are summarized in Table 4.3.

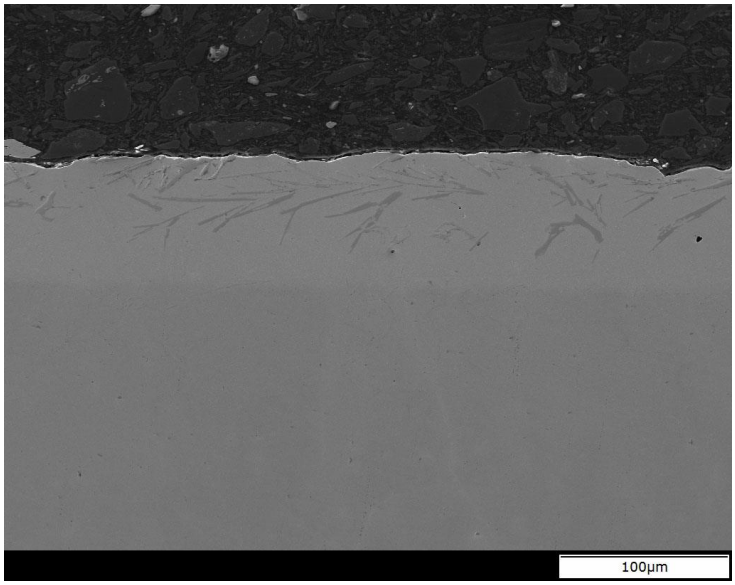

Figure 4.4- The interface position is visible in the sample held at 1524 K for five (5) minutes (lighter horizontal layer near top). The acicular phases in the upper region are likely various borides.

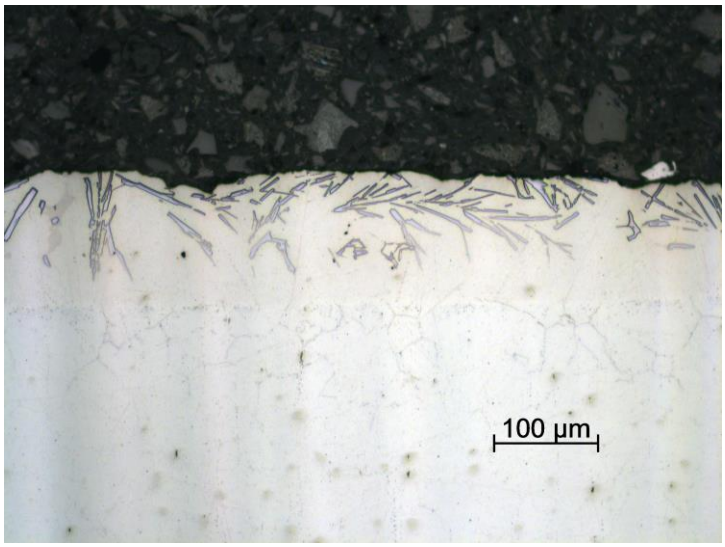

Figure 4.5- An optical photomicrograph of the Figure 4.4 sample is shown to further resolve various features.

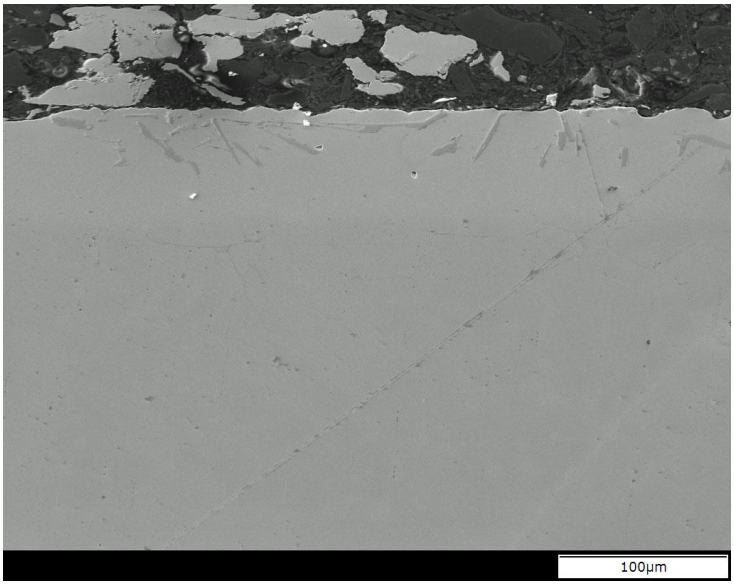

Figure 4.6- The sample held at 1523 K for ten (10) minutes is shown.

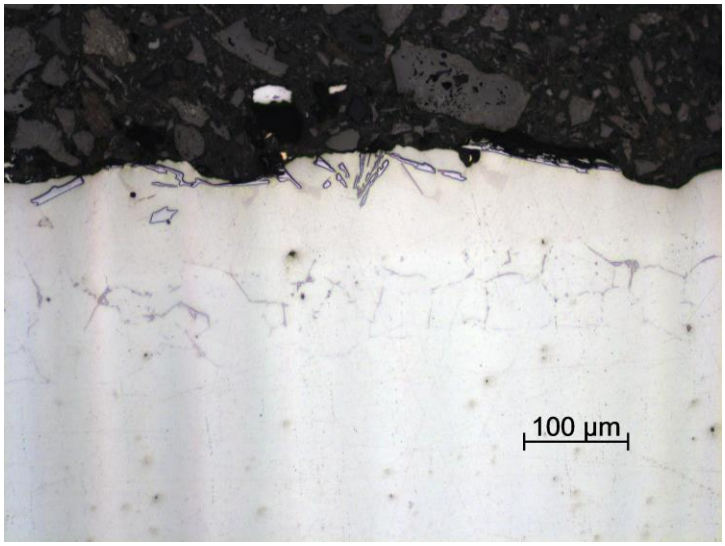

Figure 4.7- An optical photomicrograph of the Figure 4.6 sample is shown to further resolve various features.

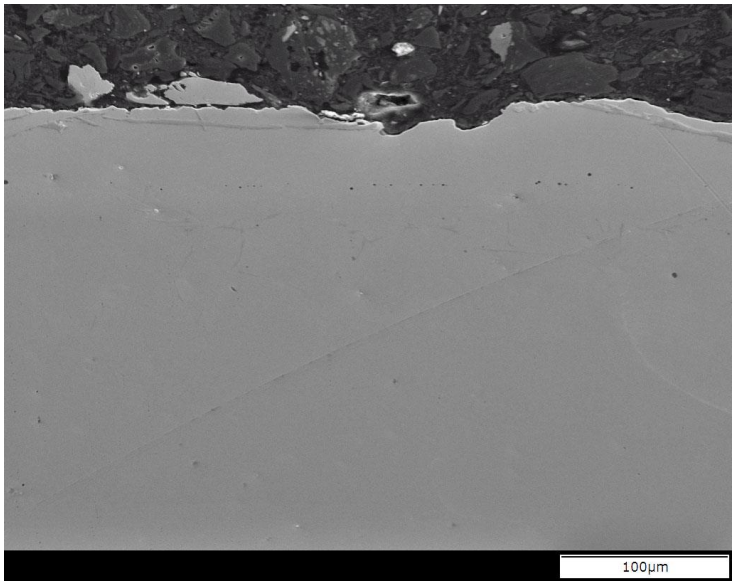

Figure 4.8- The sample held at 1523 K for fifteen (15) minutes is shown

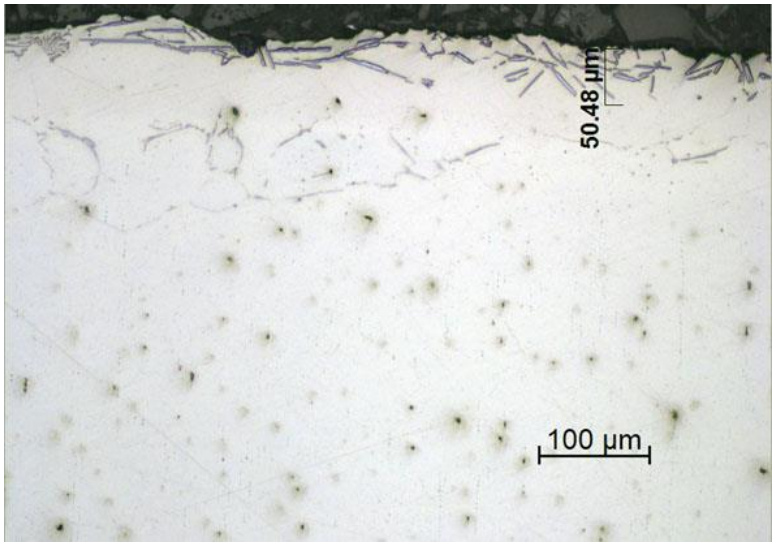

Figure 4.9- An optical photomicrograph of the Figure 4.8 sample is shown to further resolve various features.

Table 4.3**- Visually Estimated Interface Positions – **Isothermal Hold at 1523K

Time, seconds	Visually Estimated Average Position of Interface, microns	
	Assumption of all Eutectic Solidification	(Eq. 19) Using Ni-B Phase Diagram
300 (Figs. 4.4 and 4.5)	76.0	85.1
600 (Figs. 4.6 and 4.7)	66.5	74.5
900 (Figs. 4.8 and 4.9)	54.2	60.7

Method 3

The iron composition profiles of the sample brazed at 1523K (discussed in Section 4.3) are similar regardless of the isothermal hold time indicating an approximately constant interface composition. The horizontal shifting of the profiles as a function of time, therefore, can be used to estimate the interface position. The results of this method are shown in Table 4.4.

***Table 4.4**- Summary of Estimated Interface Positions Based of Fe Composition Profile*

Time, seconds	Estimated Position of Interface, microns
300	52
600	52
900	32

Methods 1 and 3 give reasonable values for the interface positions. Method 2 results in a much greater amount of widening than would be expected as when compared to expectation and Method 3. The results are consistent with expectations for the maximum gap widths; however, especially when using the correction proposed by Eq. 19. This highlights the uncertainty in using metallographic methods of measurement documented by other researchers.

4.3 Determination of Composition Profiles

Energy dispersive spectroscopy was used to determine the chemical composition profiles of the samples brazed at 1523K (braze cycle #2). The EDS was configured in the line scan mode and readings were taken over an approximately 4 mm^2 area of the polished cross sections (4 mm wide X 1 mm deep) starting at the foil edge and scanning every 2.7 microns until a depth of 100 microns was reached. The resultant concentration profiles are shown in Figure 4.10

Only minimal changes in the concentration profiles are apparent between the samples held for 360 and 3600 seconds; however, the sample held for 18000 seconds reveals significant diffusion of the silicon as well as advance of the isothermal solidification front, as evidenced by the horizontal shift in the iron and nickel profiles.

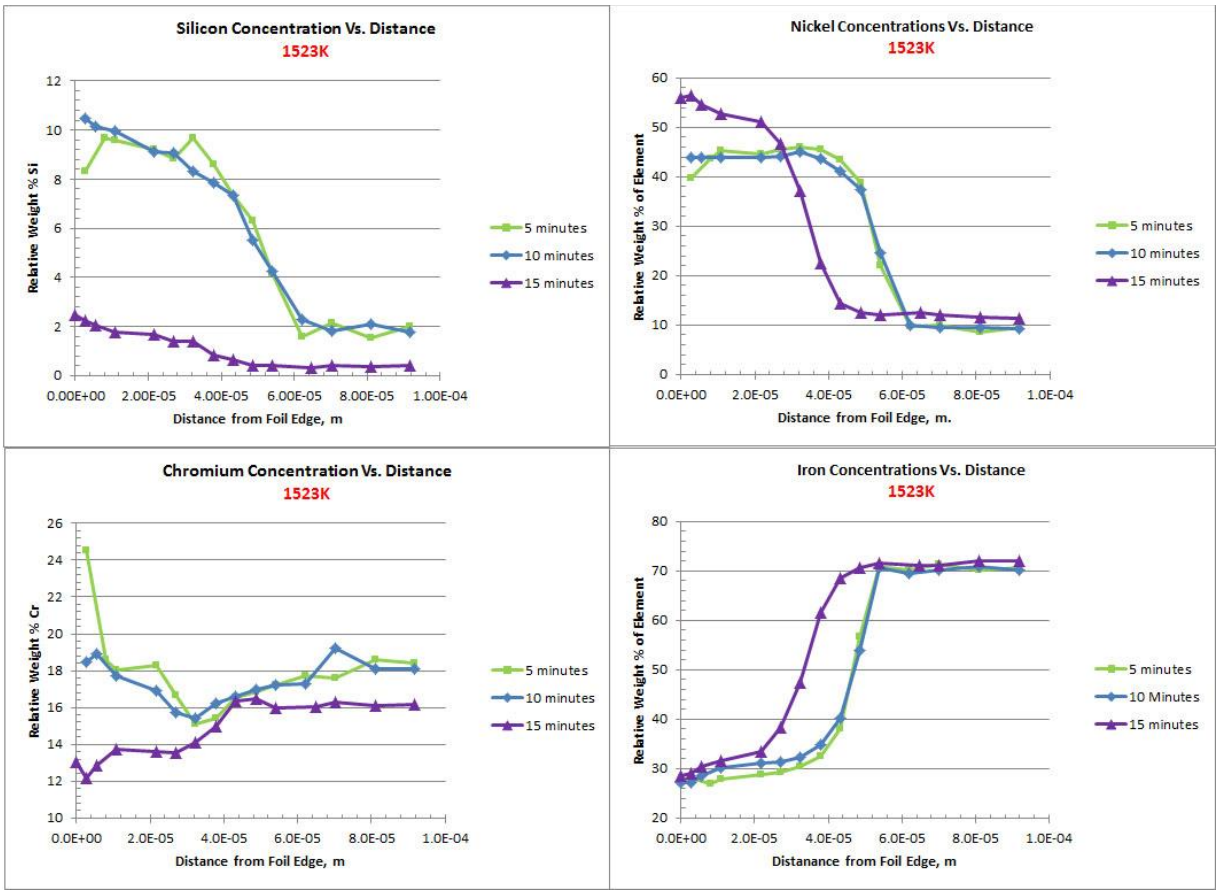

Figure 4.10- The EDS concentration profiles for silicon, chromium, iron, and nickel.

The visually apparent acicular features in the metallographic cross sections were also evaluated with EDS and exhibit elevated chromium, which is consistent with boride phases, as detailed in Table 4.5.

***Table 4.5**- Chemical Composition of Acicular Phases*

Relative Weight Percent of Element					
Reading	**%Si**	**%Cr**	**%Fe**	**%Ni**	**%Mo**
1	0.05	74.53	21.9	2.65	0.87
2	3.17	57.37	22.82	15.75	0.9
3	N.D.	81.2	12.22	2.05	4.53
4	1.27	73.68	17.38	4.75	2.92

N.D.: Not Detected

5. Numerical Simulation Methods

Thermodynamic modeling of the both the substrate and interlayer materials was performed with Thermo-Calc for Windows-Version 5 and the TLP solidification kinetics with DICTRA, which references the necessary thermodynamic databases and calculations via Thermo-Calc. To understand the simulation outputs, some basic concepts are helpful and will be discussed in the corresponding sections before simulation discussion of the simulation steps. Various Thermo-Calc results are discussed inasmuch as they are needed for explanation of the variables used in the DICTRA simulations.

5.1 Thermo-Calc

5.1.1 Concepts

Thermo-Calc uses Gibbs energy minimization technique with additional algorithms that ensure the *global* minimum is determined. This prevents the system from using metastable phases based on *local* minimums, and becomes important in para-equilibrium conditions and systems with miscibility gaps. This is done by using the concept of chemical driving force. A mesh is created for each phase present representing the Gibbs energy function at the defined conditions, and the shortest distance between the various Gibbs energy surfaces and a plane created by joining all of the chemical potentials for all of the defined elements in the system, which is the common tangent plane, is defined as the driving force (Figure 5.1). When the driving

force is equal to zero, a stable equilibrium exists. For unstable or metastable phases the driving force will be less than zero [53].

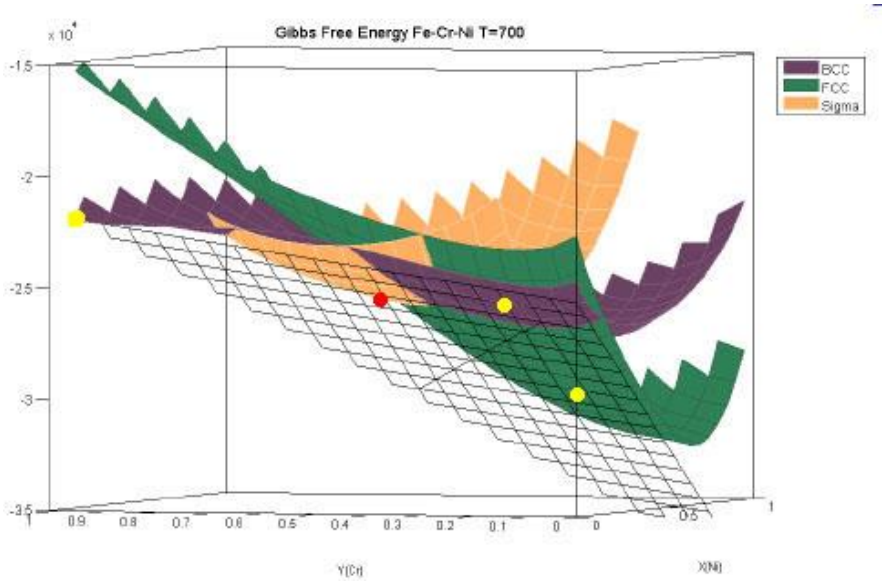

Figure 5.1- The Gibbs energy for BCC (purple), FCC (green), and sigma (orange) phases at constant temperature and composition. Local (metastable) equilibriums are shown as yellow points and the overall global equilibrium as a red point [54].

Thermo-Calc requires comprehensive descriptions of the equations of state in order to formulate the Gibbs Energy expressions and solve for equilibrium. The regular solution model with binary Redlich-Kister parameters and composition dependent ternary parameters are typically used for this [40]. Once the Gibbs Energy function for a given system is known, the value of any thermodynamic quantity can be calculated.

Recall that Gibbs Energy is always defined relative to a reference state, which is typically defined either as the same substance with the same composition at standard temperature and pressure or the most stable structure for each component in the substance at a non-standard temperature and standard pressure. Normally, the

reference state of an element in a given phase is the “pure” element at the current temperature and standard pressure [54]. In Thermo-Calc, the reference state for a component is defined by the database.

Before any of the calculations are performed, the user pulls the required thermodynamic data from a database and defines the equilibrium conditions. The thermodynamic databases are comprised of polynomial equations that describe the Gibbs Energy, which are then used to solve for the values [53].

5.1.2 Procedure

The Type 316L and MBF-51 materials were defined by entering the compositions of ICP-OES chemical analyses, as shown in Figure 5.2.

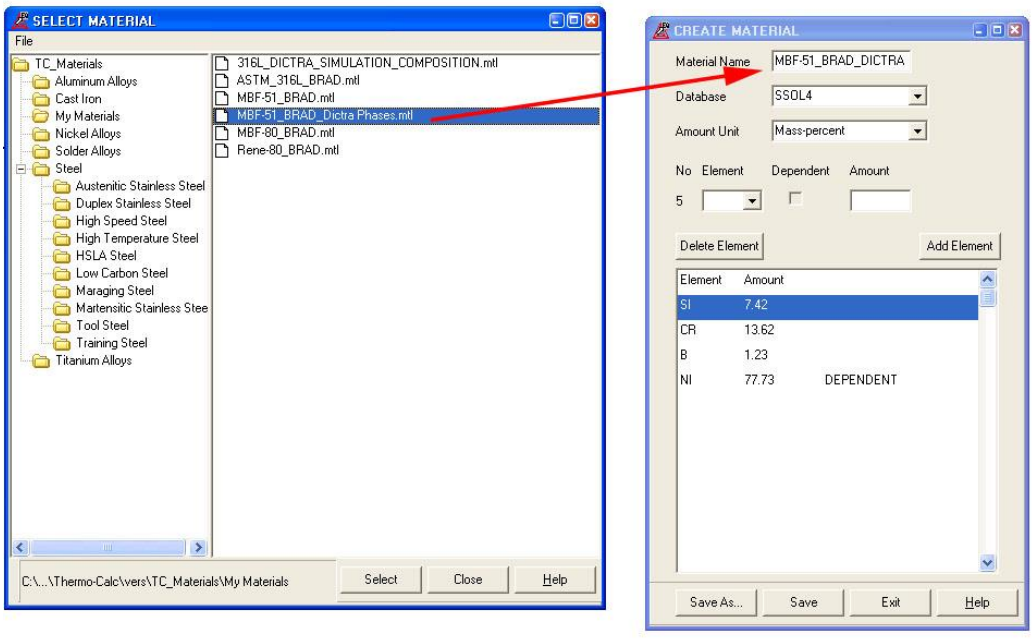

Figure 5.2- A material system was defined by direct input of the chemical compositions.

After entering the compositions of the materials, the equilibria of various phases can be studied via single-point calculations, property diagrams (single axis step), or isopleths (diagram map), as shown in Figure 5.3.

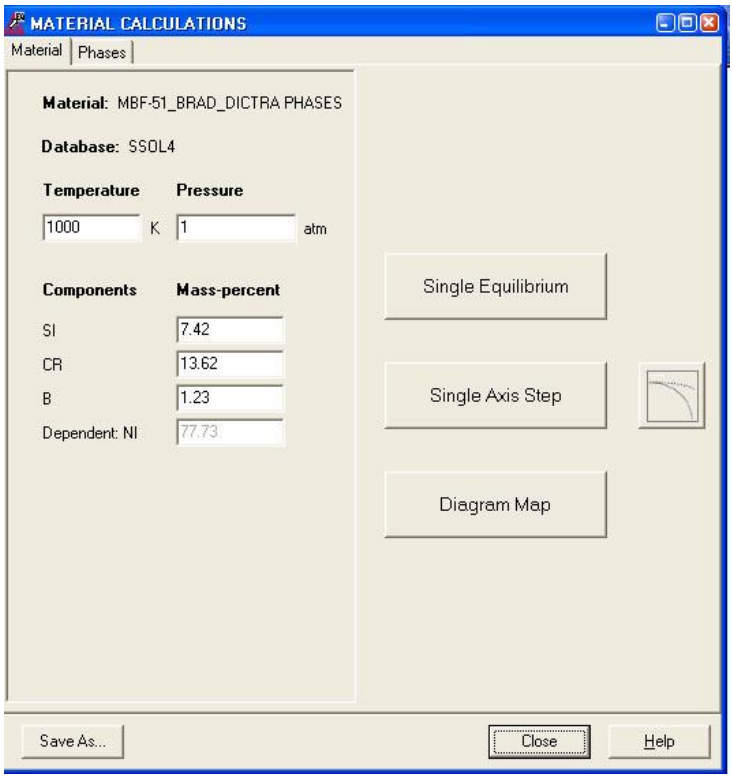

Figure 5.3- After defining an alloy system, the equilibrium calculations can be viewed as single-point calculations, property diagrams (single axis step), or isopleths (diagram map). The button on the far right is for performing a Scheil-Gulliver solidification prediction.

In the current investigation, the primary interest was characterizing the materials during diffusion processes and, therefore, predicting the expected equilibrium phases at various temperatures was necessary. The isopleths obtained for the substrate and foil materials are shown in Figures 5.4 and 5.5, and from them one can obtain a general idea of the effect of various additions/depletions of alloying elements. Note that, while an isopleth is helpful in the visualization of complex multicomponent systems, it cannot be

manipulated in the same ways as a binary phase diagram; e.g. the lever rule is not valid on an isopleth because the tie lines for may not lie in the plane of the diagram. If a degree of freedom is eliminated by taking a vertical “slice” is through the diagram at a set composition; however, the stable phases and phase amounts can be determined as a function of temperature – this is represented by a property diagram (single axis step).

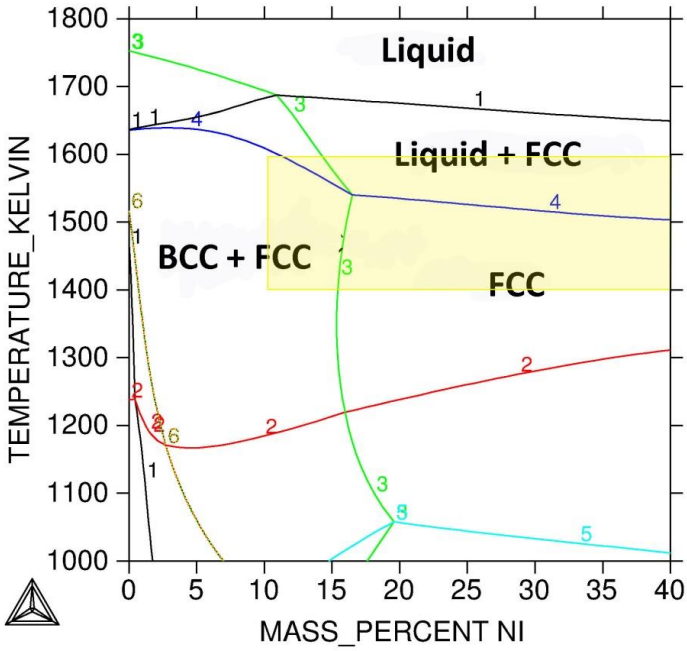

Figure 5.4- Isopleth calculated from the compositions detailed in Table 2.1 for the Type 316L substrate material. The light yellow shaded box bounds the composition and temperature ranges studied in this investigation.

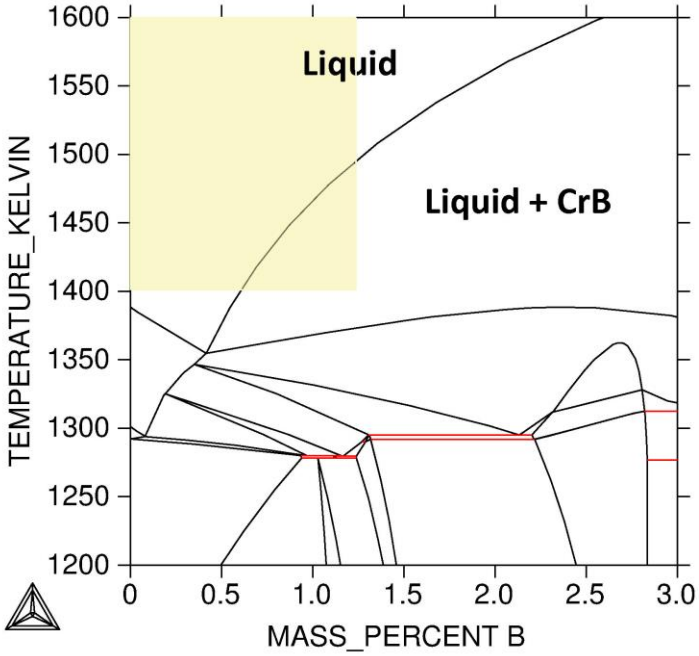

Figure 5.5- Isopleth calculated from the compositions detailed in Table 2.1 for the MBF-51 interlayer material. The light yellow shaded box bounds the composition and temperature ranges studied in this investigation.

5.1.2 Calculations

In the interest of simplifying the Dictra simulations, calculations were performed in Thermo-Calc to determine which elements, in either the substrate or braze material, could be eliminated with minimal effect on the diffusion simulation. To do this, thermodynamic diagrams were constructed for both materials, omitting different elements or combinations of elements until a composition with the lowest number of elemental species that still contained all of equilibrium phases of the "full" composition in the necessary temperature range, namely: iron, nickel, silicon, chromium, and boron.

To illustrate that altering of the substrate material from the “full” composition to the “simulation” composition has minimal effect, various comparisons are detailed in Figures 5.6 and 5.7.

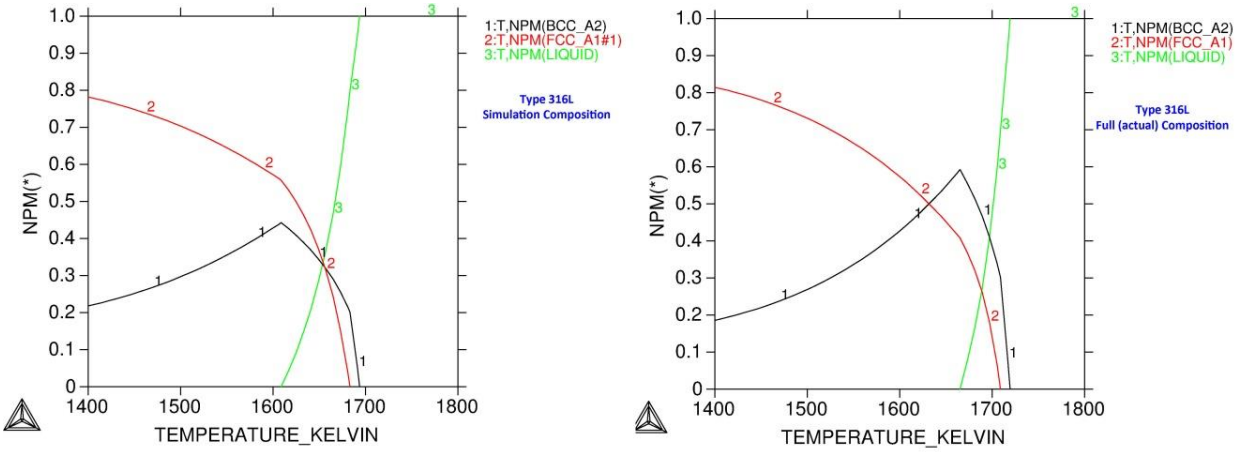

Figure 5.6- Property diagrams illustrating the total molar phase amounts for the “simulation” (left) and “full” (right) compositions of the Type 316L substrate as a function of temperature.

Table 5.1 *– Single Point Calculations Pertaining to Figure 5.6*

Temperature, Kelvin	Relative Mol % of Equilibrium Phase					
	BCC			FCC		
	316L Actual Composition	316L Simulation Composition	MBF-51	316L Actual Composition	316L Simulation Composition	MBF-51
1650	34.17	54.82	0	36.69	45.18	0
1600	42.82	42.67	0	57.18	57.33	0
1550	35.52	33.60	0	64.48	66.4	0
1524	32.43	29.86	0	67.57	70.14	0
1500	29.68	26.89	0	70.32	73.11	0
1450	25.17	22.01	0	74.83	77.99	0
1424	23.29	20.05	0	76.71	79.95	0
1374	20.45	17.20	0	79.55	82.8	0
1324	18.52	15.35	0	81.48	84.65	45.22

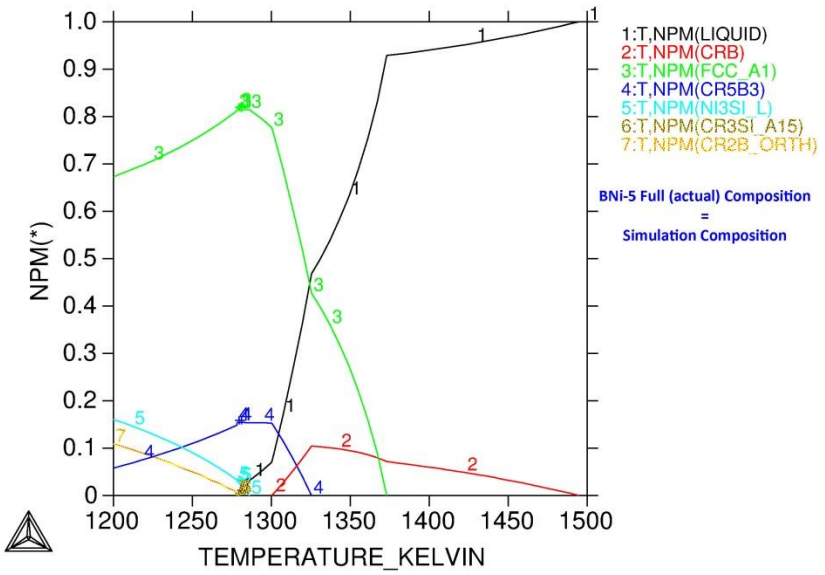

Figure 5.7- Property diagram illustrating the total molar phase amounts for the MBF-51 interlayer as a function of temperature.

Table 5.2 *– Single Point Calculations Pertaining to Figure 5.7*

Temperature, Kelvin	Relative Mol % of Equilibrium Phase					
	Liquid			Boride Phases (Combined)		
	316L Actual Composition	316L Simulation Composition	MBF-51	316L Actual Composition	316L Simulation Composition	MBF-51
1650	29.14	0	100	0	0	0
1600	0	0	100	0	0	0
1550	0	0	100	0	0	0
1524	0	0	100	0	0	0
1500	0	0	100	0	0	0
1450	0	0	96.76	0	0	3.24
1424	0	0	95.22	0	0	4.78
1374	0	0	92.90	0	0	7.1
1324	0	0	43.94	0	0	20.68

The intermediate boride phases that are known to form due to eutectic solidification of Ni-B alloys are not included in the current Dictra kinetic database; however, these may have a significant effect on kinetics of an actual system as detailed by Arafin, et. al. [16, 55]. The predicted equilibrium amount of borides in the current MBF-51 alloy system is shown in Figure 5.8 as a function of temperature.

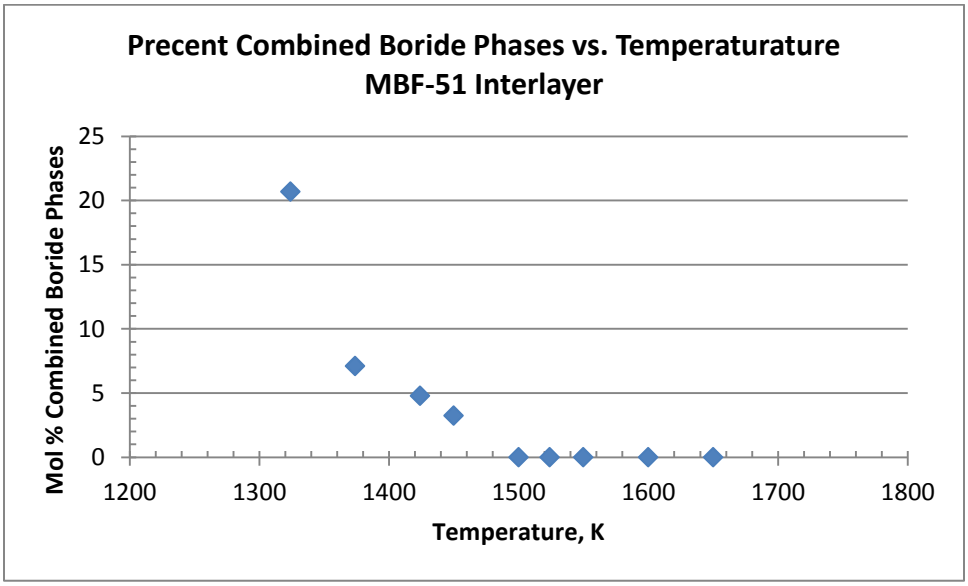

Figure 5.8- The combined mole percent of all boride phases that are thermodynamically stable for the current composition as a function of temperature.

5.2 DICTRA

5.2.1 Concepts

DICTRA employs finite difference methods to simulate one-dimensional diffusion in multicomponent alloys using a sharp interface method (Figure 5.9), which assumes a discontinuous property change at the phases interface(s) [56]. DICTRA uses a fixed-volume frame of reference and, because the molar volume of a phase varies with composition, the rate of a given phase transformation is estimated by the rate of volume diffusion of the components – this rate of volume diffusion is effectively the mass flux and can be determined with Fick's laws [57].

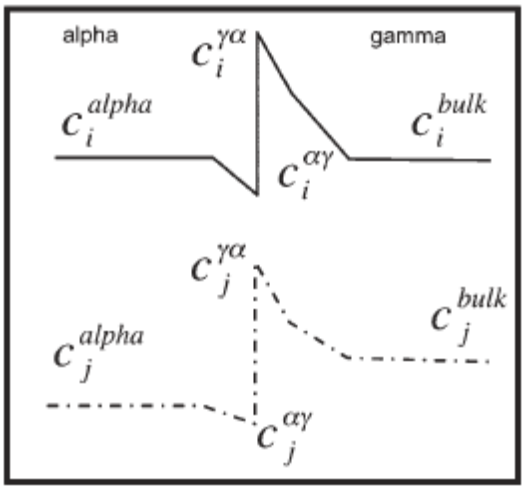

Figure 5.9- Illustration of steps in a hypothetical concentration profile due to the assumption of local equilibrium at the interface and the use of a sharp interface method [42].

During a simulation, DICTRA solves the necessary equations of thermodynamic equilibrium and uses atomic mobilities from kinetic databases to solve for the diffusion coefficients. After this, DICTRA performs three (3) primary tasks: solution of the necessary flux balance equations, solution of the diffusion equations, creation of appropriate grid points and other output variables.

Diffusion is treated in terms of chemical potential gradients. The Diffusion coefficients are calculated from the known atomic mobilities and the second derivative of the Gibbs energy (obtained from equilibrium calculations); i.e.:

$$D \sim M\left(\frac{\partial^2 G}{\partial C^2}\right)$$

Then D is substituted into Fick's 1st law to solve for flux, followed by the substitution of this flux into Fick's 2nd law to solve for the concentration gradient.

DICTRA defines a fixed-volume system as a "cell". In the current investigation, the cell defines a closed system – no energy or mass transfer in or out. The cell boundaries are thus the global boundaries for the simulation. Within the cell boundaries, one (1) or more "regions" are defined, which contain the phases. When dealing with multiphase alloys, the phases must be either separated into multiple adjacent single-phase regions that become active or inactive based on user defined conditions, or be present as a dispersed phase in the matrix phase. Unless model specific conditions are defined, diffusion is assumed to occur only in the matrix phase. The placement of the regions (phases) in the cell and how those regions are defined implicitly determines the type of diffusion model Dictra will employ: homogenization, dispersed-system, adjoining cells, coarsening, cooperative growth, or moving boundary. In the current investigation, the moving boundary model is used.

The moving boundary model consists of two (2) regions, each consisting of one (1) phase, as shown in Figure 5.10. Movement of the interface separating the regions is determined by the amount and direction of diffusive flux at the interface, which is a mass balance. Equilibrium is assumed at the phase interface so that the phase distribution and composition can be calculated from phase diagram information. In

other words, the elemental concentrations at the interface are given by the ends of the tie-line on the phase diagram, as previously discussed in Section 2.

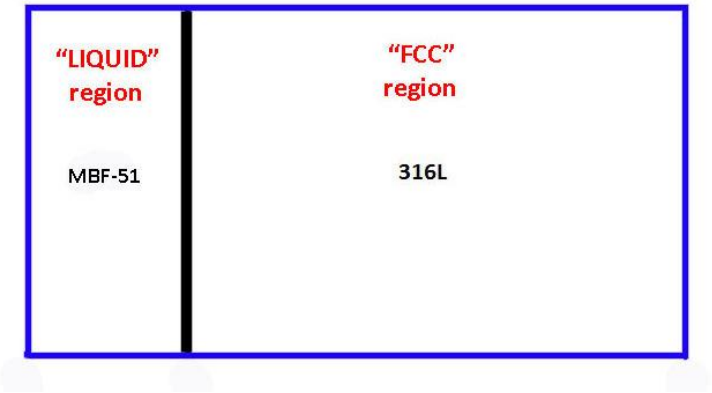

Figure 5.10- The regions used in this investigation are identified according their initial phase: liquid MBF-51 and FCC (solid) 316L. The regions are present in a closed "cell" (blue outline) and interact with one another at the shared interface (vertical black line).

The user defines the number and distribution of "grid points" that are placed along the axis. The software determines the local equilibrium at each grid point, which the subsequent thermodynamic and kinetic equations are based upon.

5.2.1 Assumptions and Boundary Conditions

- The initial heating of the system and subsequent melting of the filler metal were not included in the simulation as preceded by many other researchers [43].
- The simulations began at the isothermal hold temperature with a fully liquid MBF-51 interlayer region and a fully solid 316L substrate region. Furthermore, based on the phase stability information obtained from Thermo-Calc, the solid substrate is assumed to consist completely of the face centered cubic (FCC) phase.

- Movement of the interface is controlled by mass balance requirements, which is dependent on the diffusive flux of individual elements at the interface.
- Local equilibrium is maintained at the interface – this means that the *net* flux is zero. Because this is a multicomponent system, the tie-line used for calculations is determined by the condition that the mass balance of every diffusing element has the same interface velocity.
- One-dimensional geometry; i.e. no grain boundary diffusion.

5.2.3 Procedure

Iron, nickel, chromium, silicon, and boron were used to define the systems thermodynamic (SSOL4 database) and kinetic (MOB2 database) parameters. All of the diffusion simulations used the moving boundary model and two (2) regions; liquid BNi-5 on the left side and FCC (solid) 316L on the right side (Figure 5.10). Each region contains one (1) active matrix phase, i.e. BNi-5 contains the liquid phase and 316L contains the FCC phase.

Most of the simulations were performed to best mimic the experimental variables and boundary conditions; however, an appreciable amount were also performed to study the effect of variability on certain parameters and can very generally be grouped according to the foil thickness used: 38 microns (experiment foil thickness), 76 microns, and 380 microns.

Position of interface and boron composition profiles (i.e. concentration gradients) were tracked in all simulations, while the composition profiles of iron, nickel, silicon, and chromium were tracked only in the 38 micron foil thickness simulations. Boron was chosen as the primary element to track because it's a relatively small interstitial "fast-diffuser" and it was hypothesized that the boron concentration profiles could therefore be used to determine the total diffused distance into the substrate.

Table 5.3 lists the more critical conditions with explanations as necessary, in hopes the reader can reproduce the results if desired.

Table 5.3 *– DICTRA Conditions Commonly Used in the Current Investigation*

Variable	Entered	Notes
Set Condition	Global Temperature	The entire system will remain at the chosen temperature
Low Time Limit	0	- - -
High Time Limit	*	no upper boundary; i.e. ∞
Grid Spacing	50 points in each region	- - -
Grid Geometry	Geometric	A prompt to enter a value of "R" for each region follows. Depending on what is chosen, the 50 points defined earlier can be concentrated near either system boundary or interface. The settings used in this investigation were almost always 0.97 for the foil region and 1.03 for the substrate, which clusters more near the interface on both sides.
Composition Type	Weight Percent	The system requires a value for all elements, if the element is not present, such as Boron in the 316L, a value of 1e-5 should be entered per the Dictra User Guide
Simulation Time	For most simulations this was set at 1.0e5 seconds (~28 hrs.)	To ensure that if complete isothermal solidification did occur within a semi-reasonable time that it would be noted
Simulation Conditions: Check Interface Position	Yes	Re-adjusts grid point distribution based on movement of the interface.
Simulation Conditions: Degree of Implicity	1	Less accuracy than the trapezoidal method (0.5) but more forgiving and allows for faster simulations.

After a simulation was completed, the data points for the Dictra post-processor generated position of interface and composition profile plots were exported to Microsoft Excel 2010 for evaluation.

The exclusion of the body centered cubic (BCC) phase was mostly due to modeling challenges – The current version of DICTRA does not have an intuitive method for dealing with two primary (i.e. matrix) phases in a single region. The models that are available to multiple phases in a region, such as a spheroidal or lamellar phase, do not apply to the current system and, therefore, the exclusion of BCC was due to the lower molar and weight percentages of BCC present at the compositions and temperatures studied in the current investigation and also because the primary equilibrium matrix phase expected upon the solidification of MBF-51 is FCC.

6. Numerical Simulation Results and Discussion

The preliminary thermodynamic calculations discussed in Section 5.1.2 indicate that some of the elements may be eliminated from the type 316L substrate material with no apparent effect on phase equilibria. This abridged composition (Table 6.1) was used for all of the discussed simulations.

***Table 6.1**- Abridged Composition Used for Simulations*

Element	Type 316L Base Material, Actual	BNi-5 (MBF-51) Braze Foil, Actual
Carbon	0.02	<0.001
Manganese	1.44	0.01
Silicon	0.58	7.42
Phosphorus	0.03	<0.005
Sulfur	0.04	<0.005
Chromium	16.07	13.62
Nickel	10.02	Remainder
Molybdenum	2.00	<0.005
Copper	0.47	<0.005
Vanadium	0.07	<0.005
Cobalt	0.11	0.05
Boron	<0.001	1.23
Iron	Remainder	0.58

The elements are highlighted as included or omitted

6.1 Position of Interface

The interface positions are shown as a function of time in Figures 6.1 through 6.3 for the 38 micron foil thickness, Figures 6.4 through 6.6 for the 76 micron thickness, and Figures 6.7 through 6.9 for the 380 micron thickness. With the exception of the 38 X 10^{-6} m foil thickness at 1600 K, all of the scenarios exhibit the expected TLP solidification behavior of widening, reaching a maximum braze gap, and shrinking of the liquid phase by isothermal solidification. Arafin [14] noted a significant decrease in isothermal solidification time with increasing temperature or decreasing interlayer thickness when studying a 410 stainless steel/BNi2 system, and many others have verified this relationship in other alloy systems as well. The results of this investigation do not appear to corroborate these findings; however, none of the simulations performed in the current investigation achieved complete isothermal solidification and so the comparison may be flawed.

The maximum amounts of dissolution, defined in terms of the liquid width (commonly referred to as the gap width), as well as the dissolution times and average dissolution rates are summarized in Table 6.1.

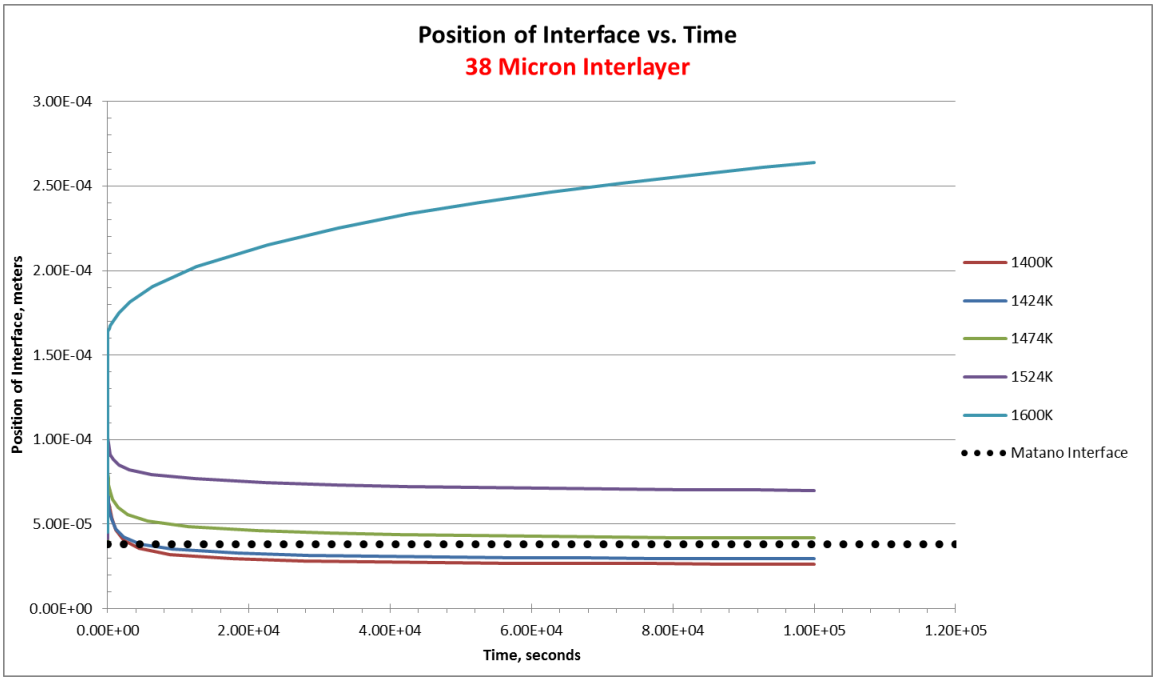

Figure 6.1- The interface position of the 38 micron interlayer simulation is plotted as a fuction of time.

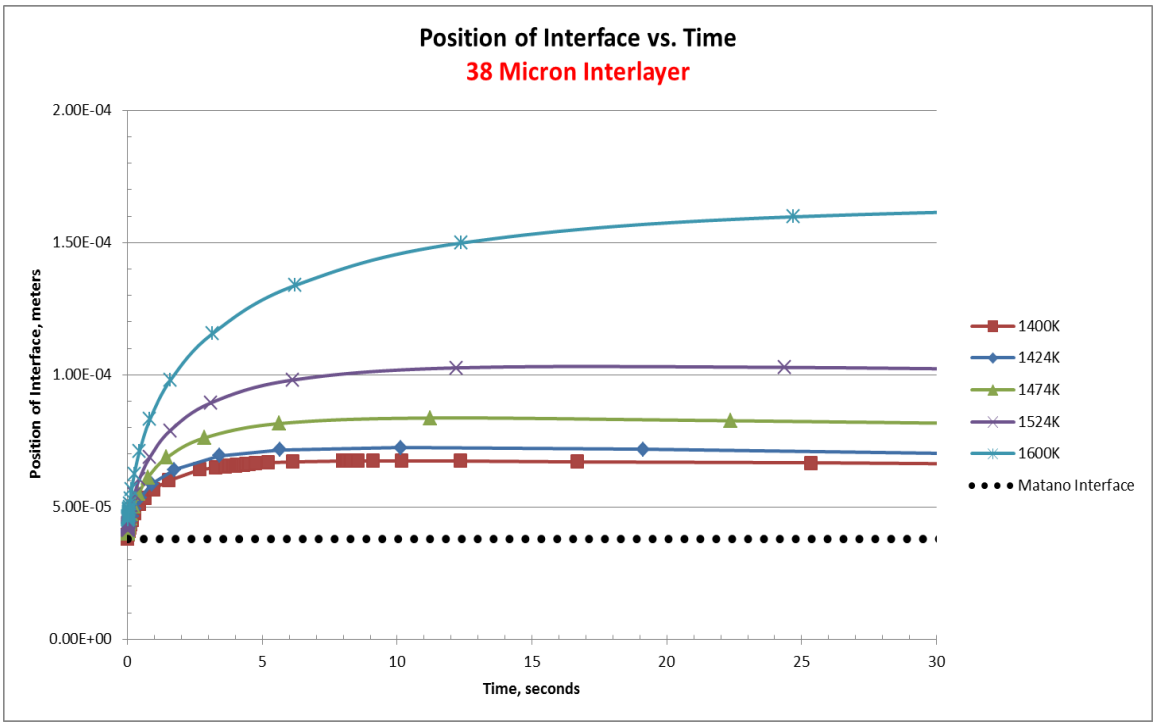

Figure 6.2- The graph shown in Figure 6.1 after scaling to better show the dissolution stage.

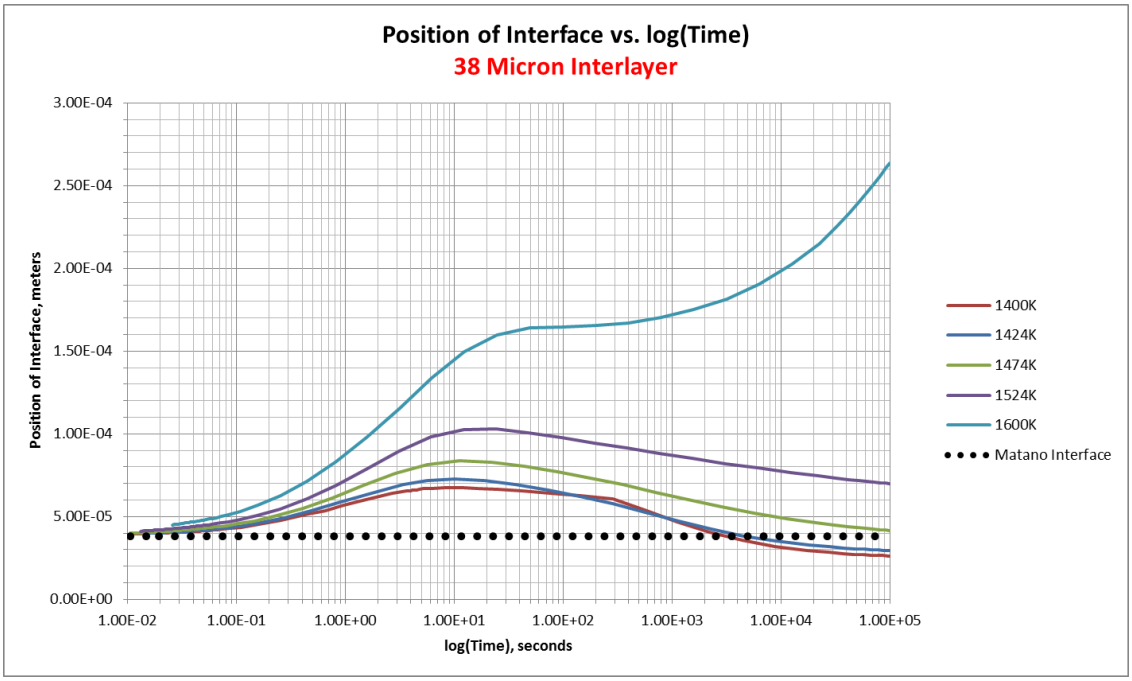

Figure 6.3- The graph shown in Figure 6.1 is plotted as a function of log(time).

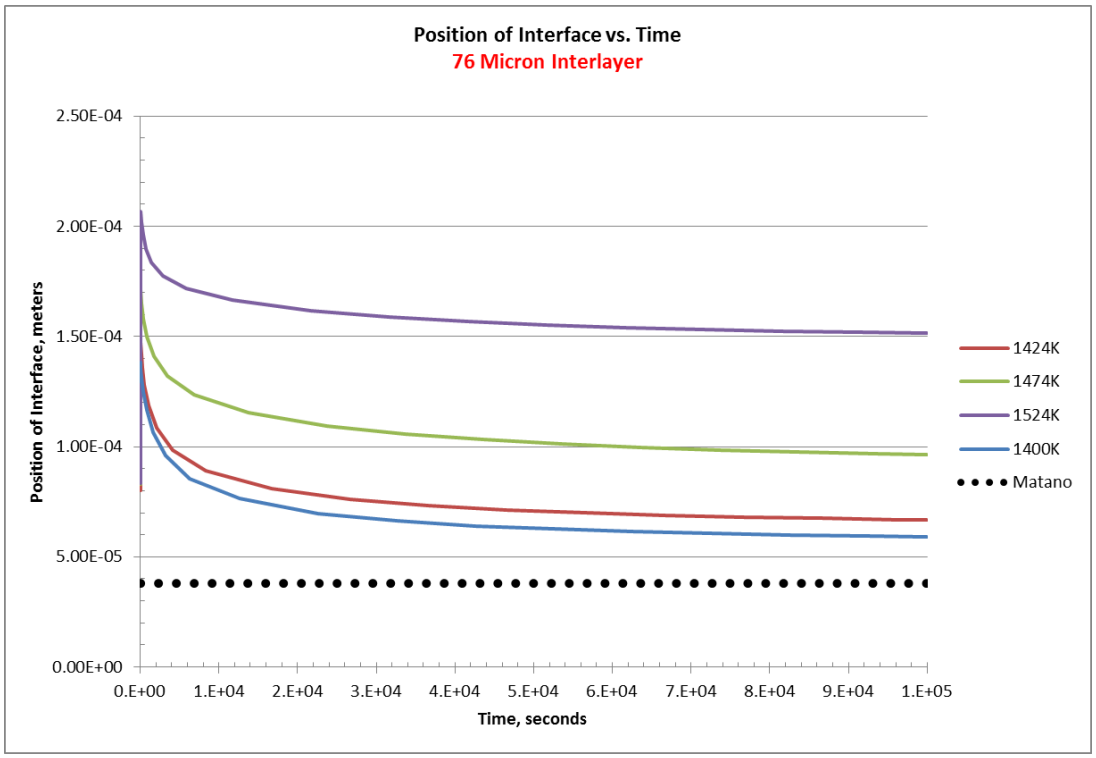

Figure 6.4- The interface position of the 76 micron interlayer simulation is plotted as a fuction of time.

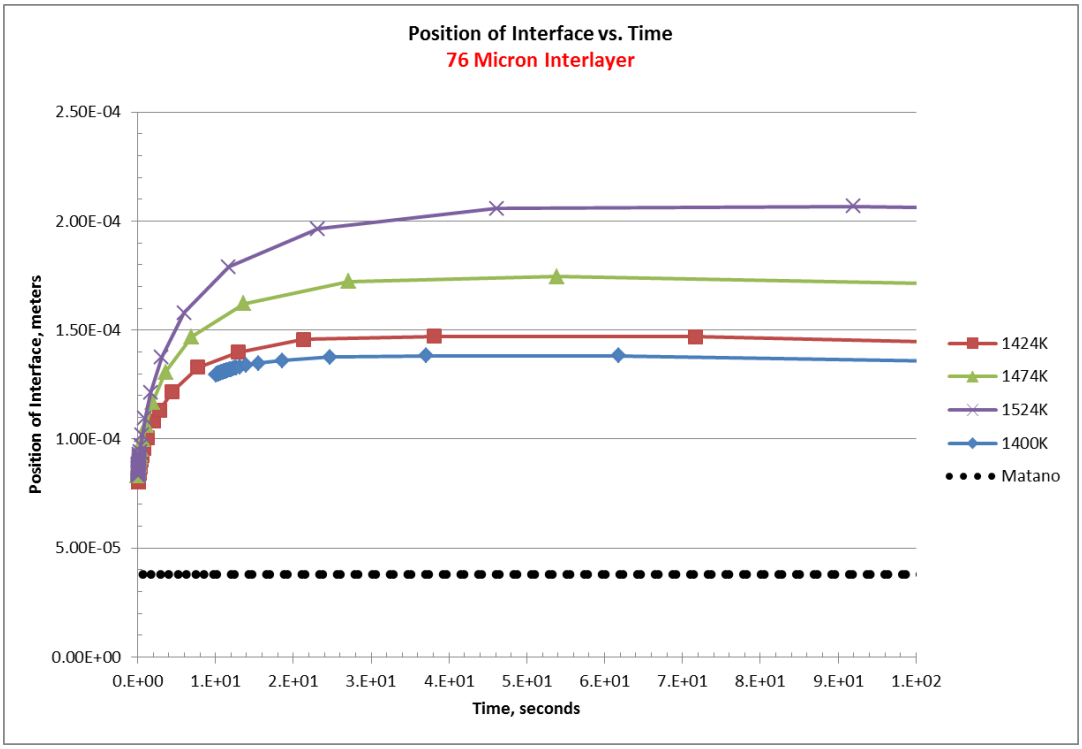

Figure 6.5- The graph shown in Figure 6.4 after scaling to better show the dissolution stage.

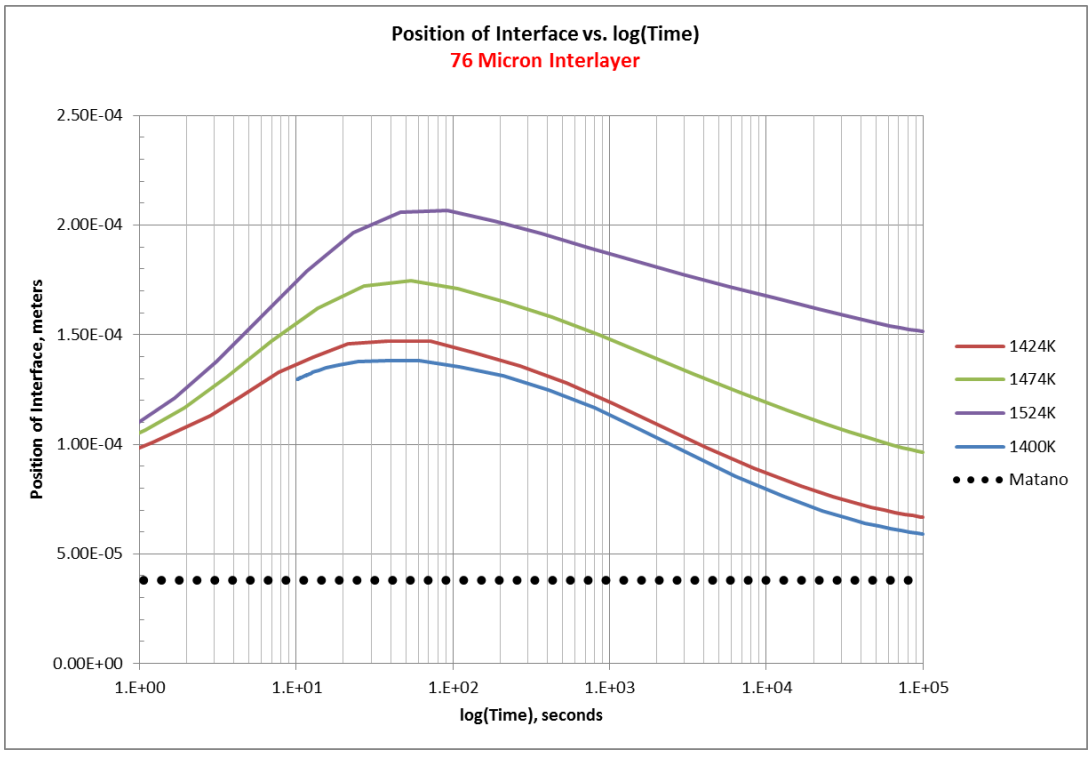

Figure 6.6- The graph shown in Figure 6.4 is plotted as a function of log(time).

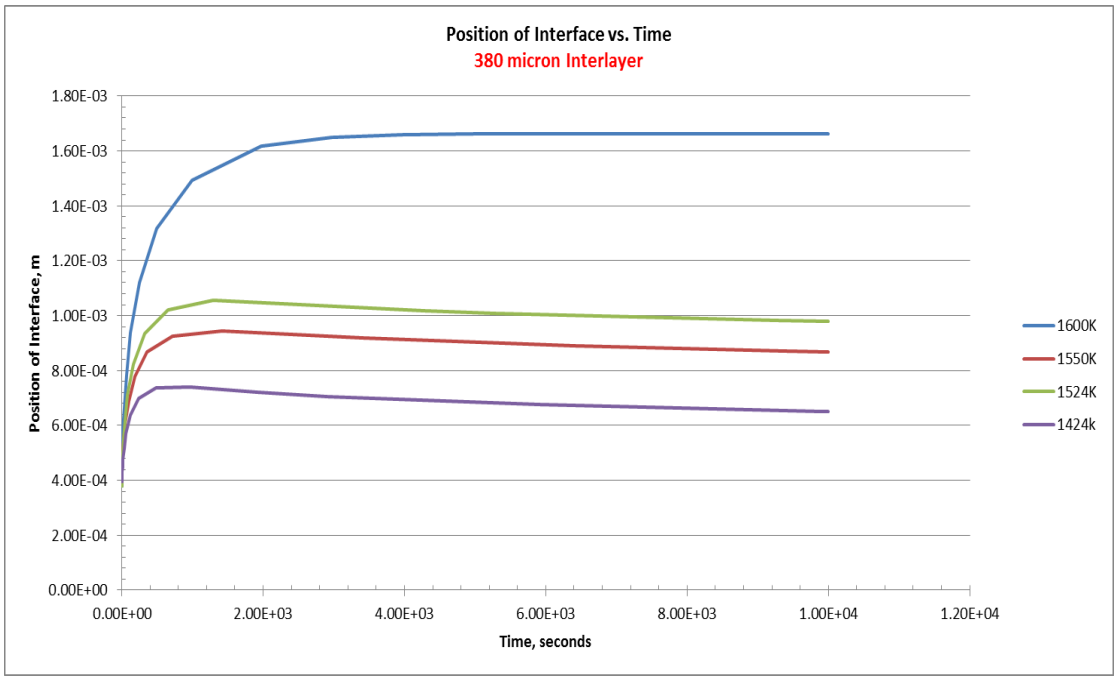

Figure 6.7- The interface position of the 380 micron interlayer simulation is plotted as a fuction of time.

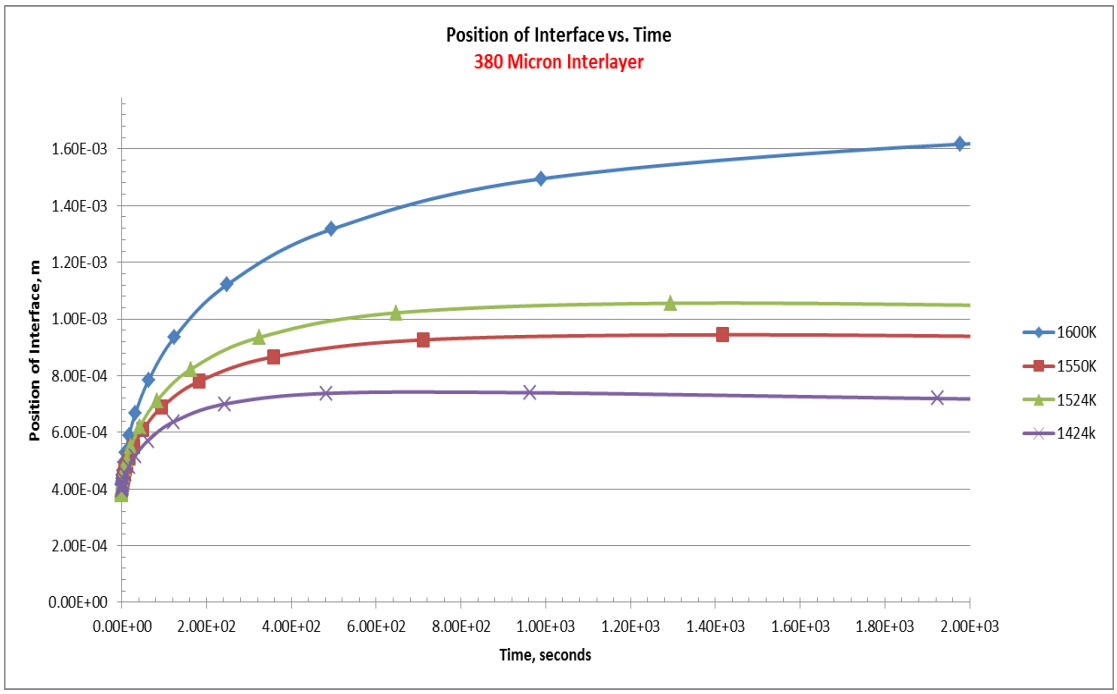

Figure 6.8- The graph shown in Figure 6.7 after scaling to better show the dissolution stage.

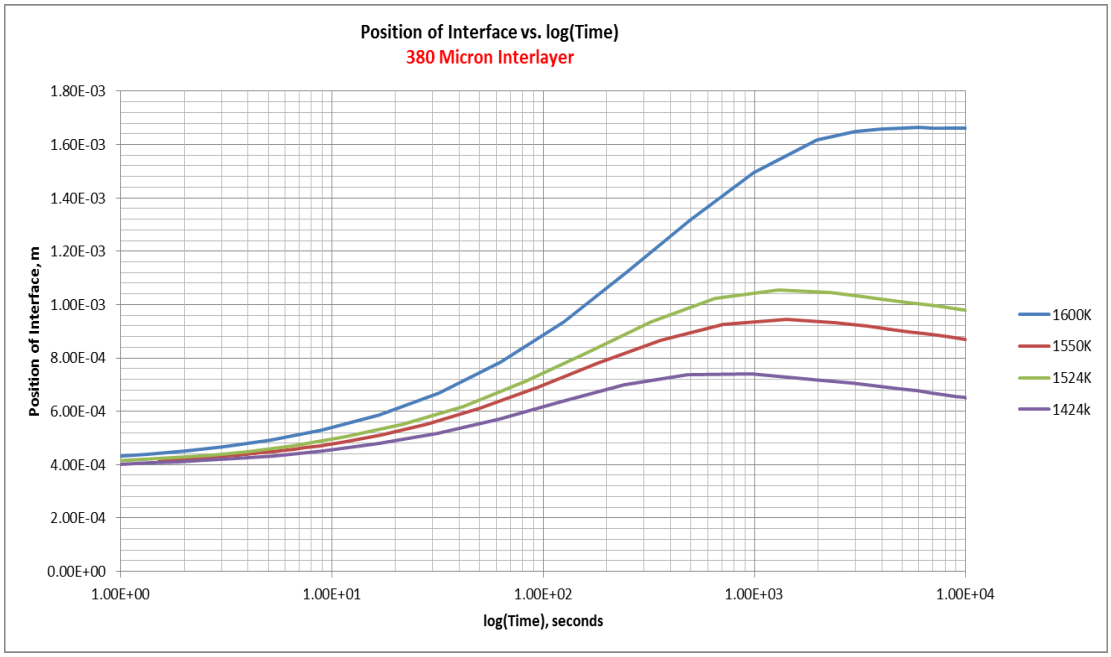

Figure 6.9- The graph shown in Figure 6.7 is plotted as a function of log(time).

Table 6.2 *– Summary of the Position of Interface Simulations*

Temperature, K	Initial Interlayer width, microns	Overall Maximum Gap Width, microns	Total amount of Substrate Dissolution, microns	Dissolution Time, seconds	Average Dissolution Rate, microns/sec.
1400	38	67.5	29.5	8.0	3.7
	76	138.3	62.3	37.1	1.7
	380	N.P.	N.P.	N.P.	N.P.
1424	38	72.5	34.5	10.1	3.4
	76	147.2	71.2	38.1	1.9
	380	740.0	360	963.3	0.4
1474	38	83.7	45.7	11.2	4.1
	76	174.6	98.6	53.9	1.8
	380	N.P.	N.P.	N.P.	N.P.
1524	38	102.8	64.8	24.3	2.7
	76	206.7	130.7	92.0	1.4
	380	1044.1	664.1	2294.0	0.3
1600	38	(1)	N.P.	(1)	N.P.
	76	N.P.	N.P.	N.P.	N.P.
	380	1663.3	1283.3	5977.0	0.2

N.P.: Simulation not performed.

(1): Widening of the liquid continued for entire simulation time; maximum gap width was not achieved.

The results indicate that the total amount of substrate dissolution is greater for thicker interlayers (Figure 6.10) and higher temperatures (Figure 6.11). Additionally, the average dissolution rate decreases as the initial interlayer width increases (Figure 6.12).

The maximum average dissolution rate does not always follow a linear relationship and is dependent on both the initial interlayer width and isothermal hold temperature. This suggests that for a given interlayer thickness, a temperature range exists that minimizes dissolution time. The findings correspond well with the reviewed literature [3, 16]. In general, others have found that the time required to reach the maximum gap width is dependent on the initial interlayer width, chemical composition, and heating rate. Thinner layers (<200 microns) exhibit less dissolution and, at lower heating rates, tend to better follow the equilibrium liquidus composition [3].

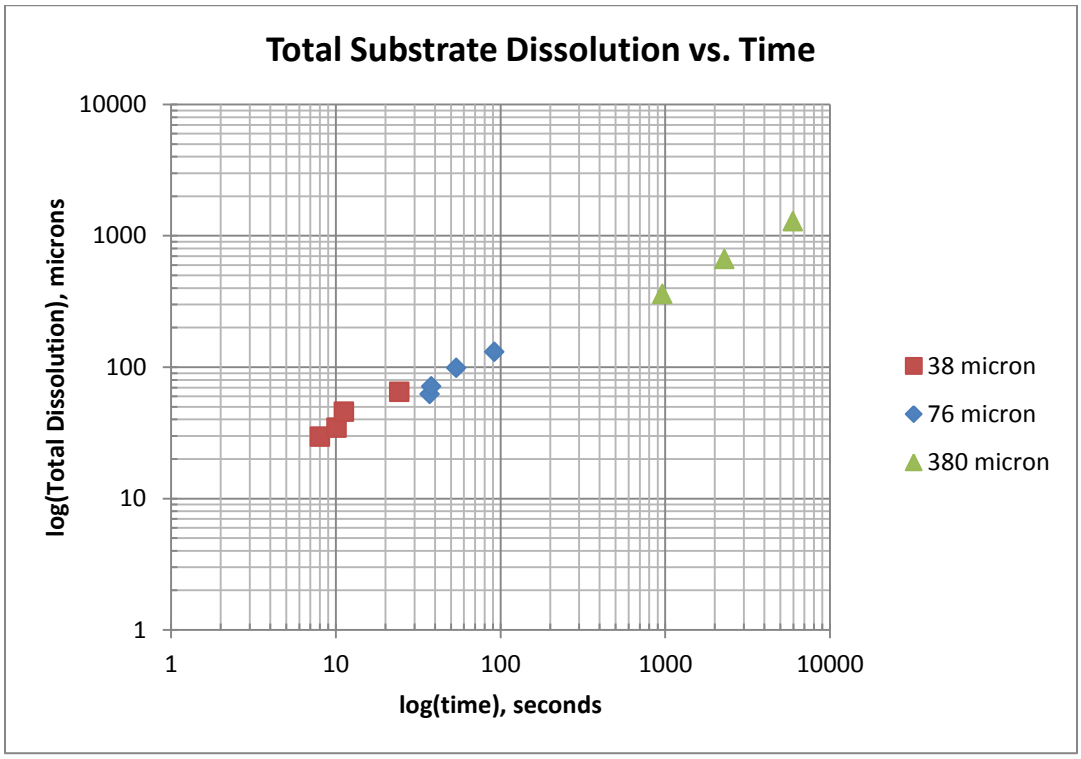

Figure 6.10- The total amount of substrate dissolution is directly related to time at temperature for all three interlayer thicknesses.

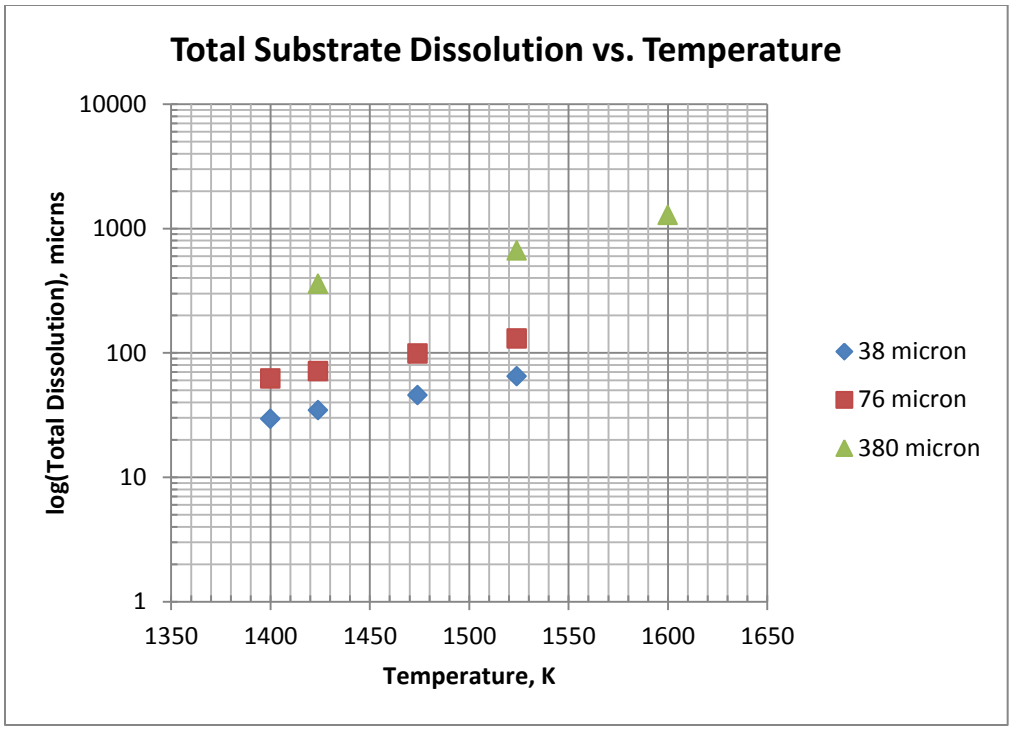

Figure 6.11- The total amount of substrate dissolution is directly related to isothermal hold temperature for all three interlayer thicknesses.

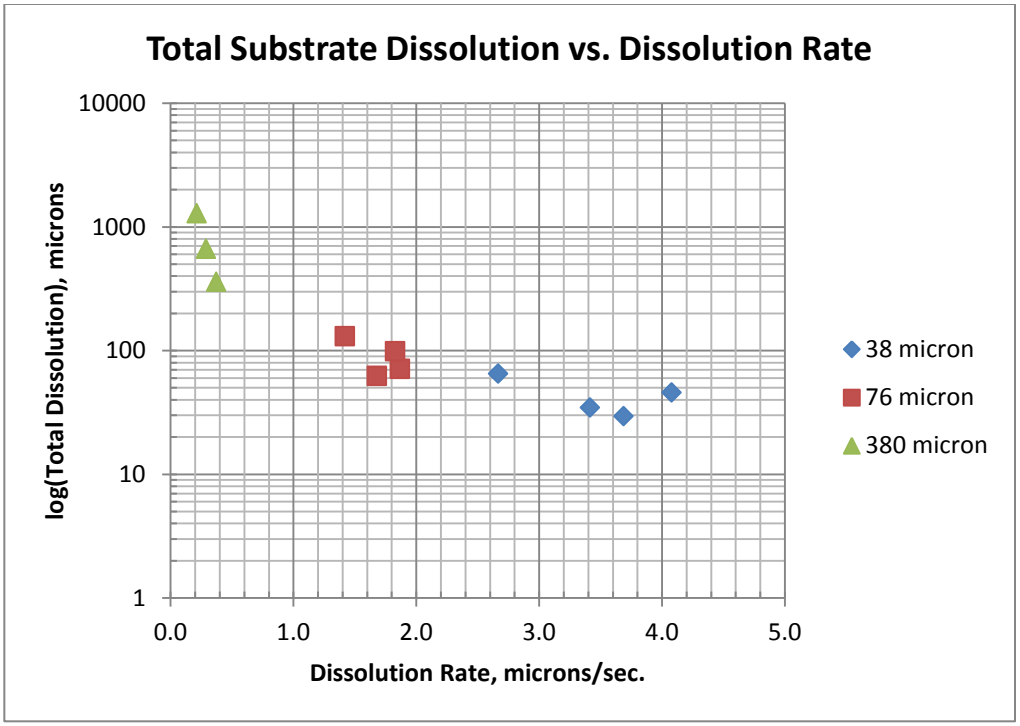

Figure 6.12- The above points reveal that maximizing the average dissolution rate depends on the temperature and is unique for a given interlayer thickness.

The simulations are consistent with other reported position of interface versus time plots with the general exception of the lack of complete isothermal solidification in any of the simulations and the specific exception of the 38 micron 1600K simulation, which appears to widen through the entire simulation time.

Both the lack of complete isothermal solidification in any of the simulations as well as the continuous substrate dissolution of by the 38 micron foil at 1600 K are likely caused by the assumption of equilibrium at the interface and the phases chosen. Figure 6.13 through 6.20 are isopleth diagrams at 1374K, 1424K, 1524K, and 1600K; respectively. The isopleths reveal the shortcomings of assuming only liquid and FCC phases in the simulations – at 1374, which was attempted but not reported due to convergence errors, the phase that was assumed liquid is actually different amounts of FCC, boride phases, and liquid, depending on the boron and silicon amounts. According to the 1600K property diagram, a fully solid structure is thermodynamically impossible even at negligible boron and silicon - the same phenomena was also noted in the 1524K and 1424K isopleths.

To better understand the consequences of iron dissolution into the liquid, thermodynamic calculations were also performed with a significant mass percentage of iron in the liquid (50 wt%). No significant changes were noted.

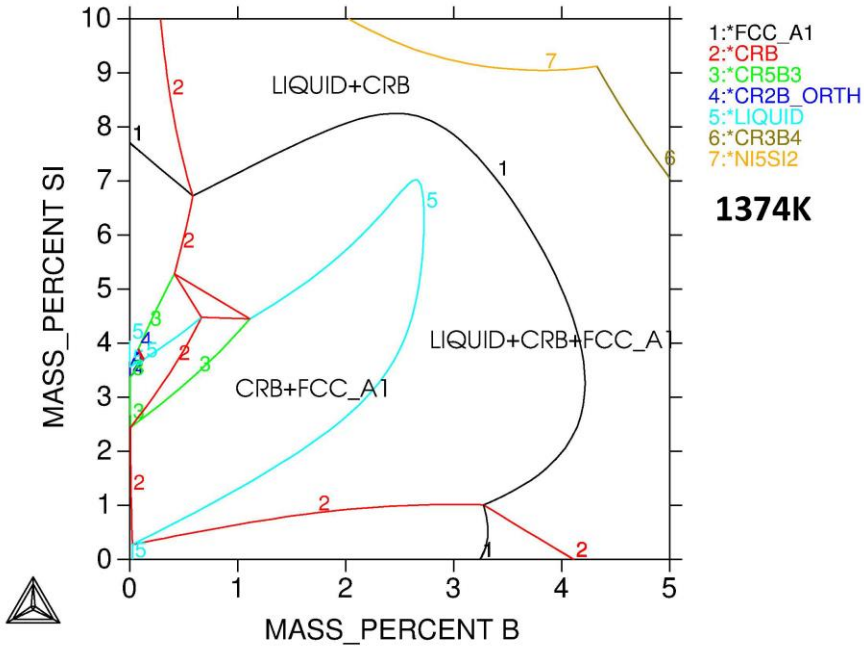

Figure 6.13- The effect of boron concentration on isothermal solidification as a function of silicon content at 1374 K.

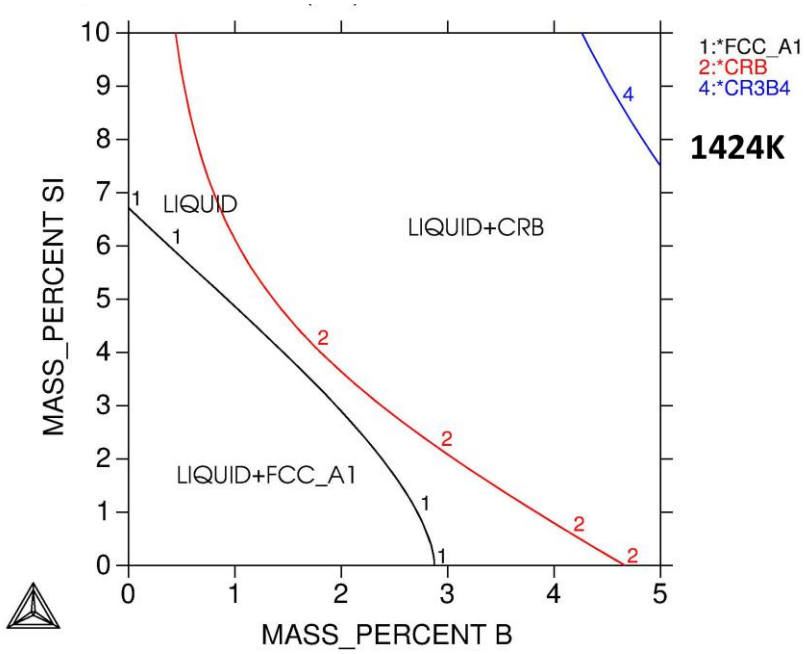

Figure 6.14- The effect of boron concentration on isothermal solidification as a function of silicon content at 1424 K.

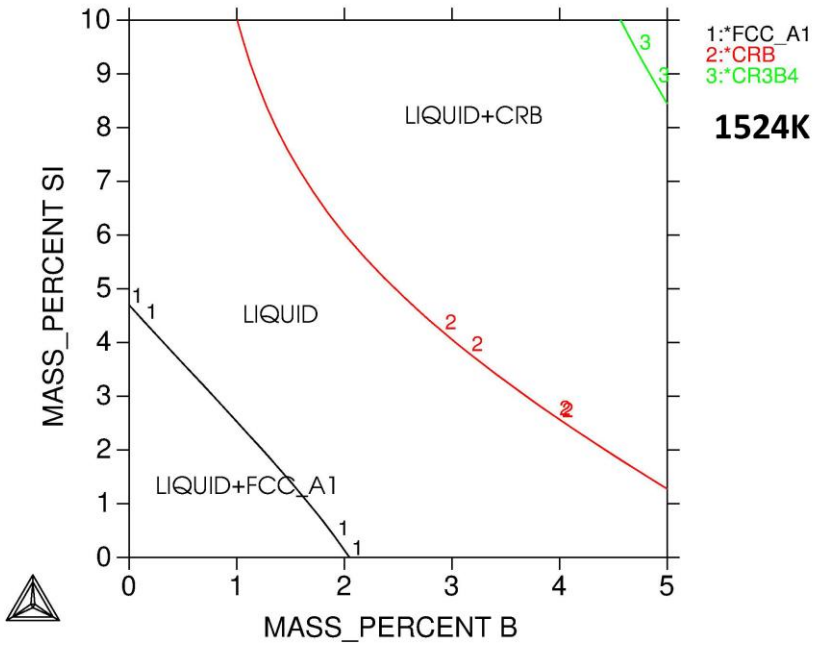

Figure 6.15- The effect of boron concentration on isothermal solidification as a function of silicon content at 1524K.

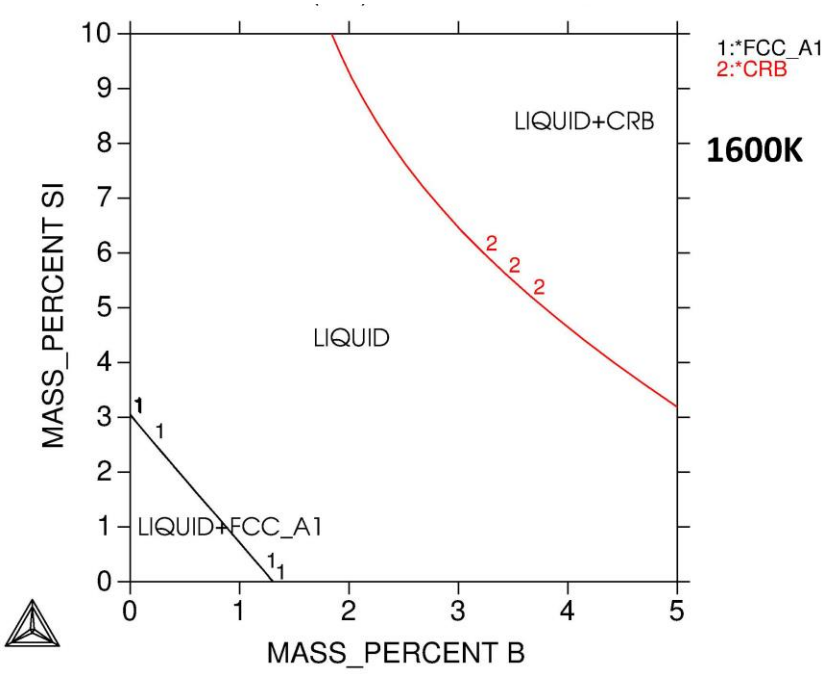

Figure 6.16- The effect of boron concentration on isothermal solidification as a function of silicon content at 1600K.

6.2 Composition Profiles

Composition profiles for the 38 micron foil thickness simulated at 1524 K are illustrated in Figures 6.17 through 6.21 for all of the simulated elements. Boron composition profiles are shown for 1424, 1474, and 1600K in Figure 6.22.

The discontinuities or, steps, in the concentration profiles are due to the assumption of equilibrium at the interface and use of the sharp interface approach method. The vertical line is the solid-liquid interface and represent a tie-line on the equilibriumphase diagram, as illustrated in Figure 6.23. In many of the profiles the steps start to occur at similar concentrations; e.g. boron between 0.4 and 0.5wt% and silicon between 2.5 and 3.0wt%. This relates to the maximum solid solubility of the elements in the solid FCC phase at the simulated temperature.

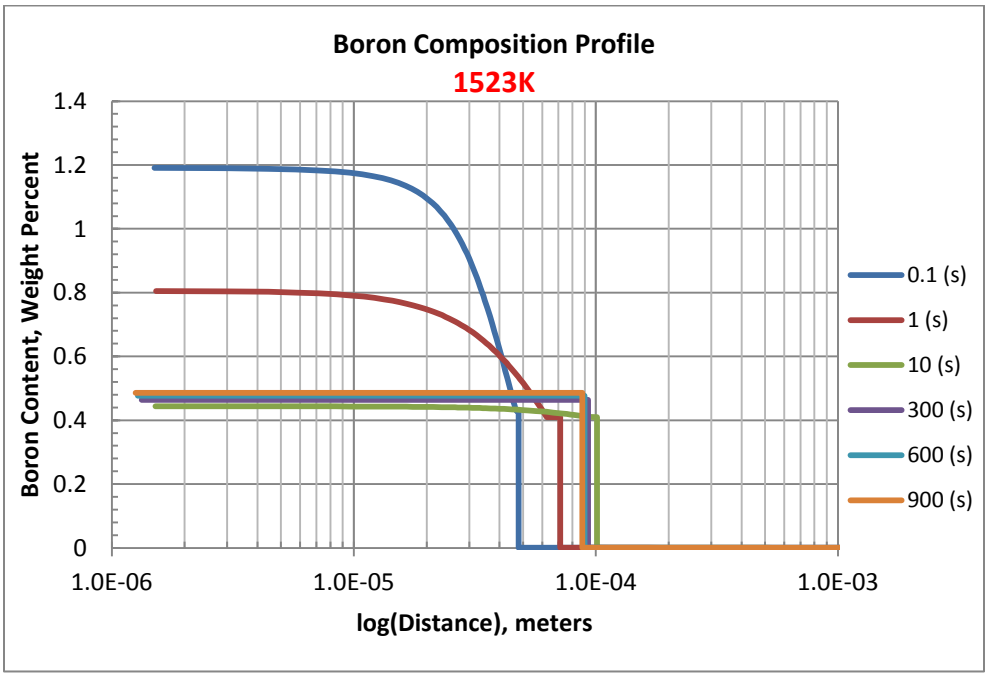

Figure 6.17- The simulated composition profile for boron is shown for various hold times at 1523K.

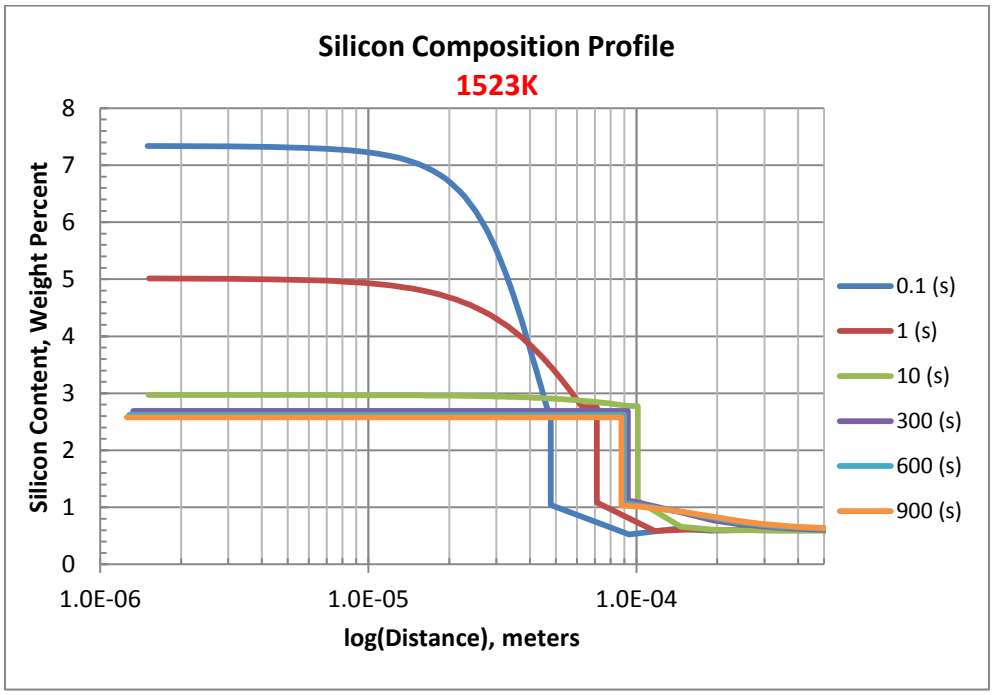

Figure 6.18- The simulated composition profile for silicon is shown for various hold times at 1523K.

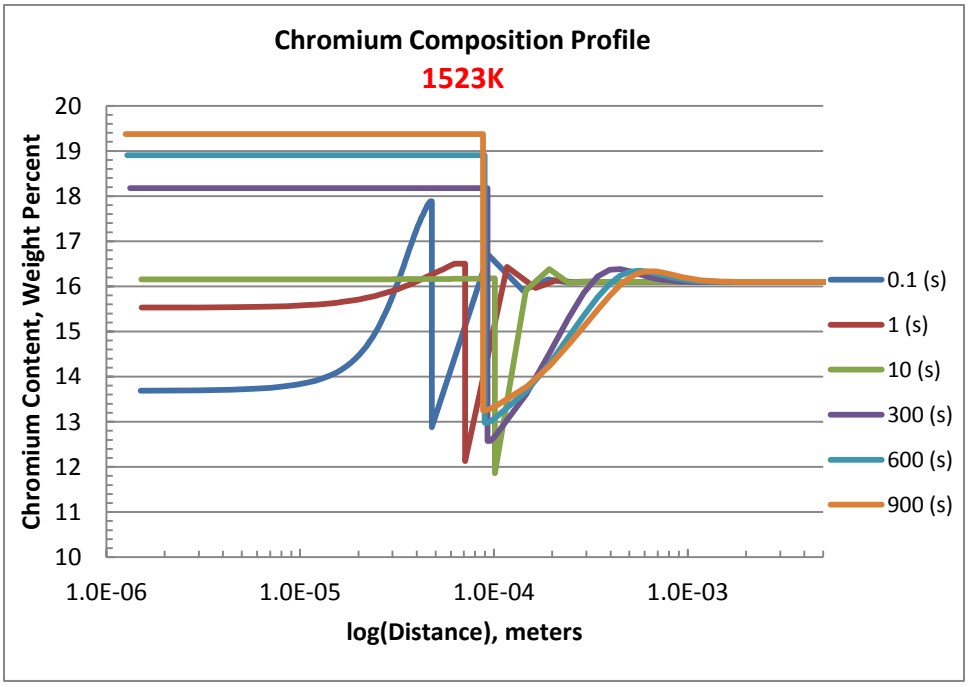

Figure 6.19- The simulated composition profile for chromium is shown for various hold times at 1523K.

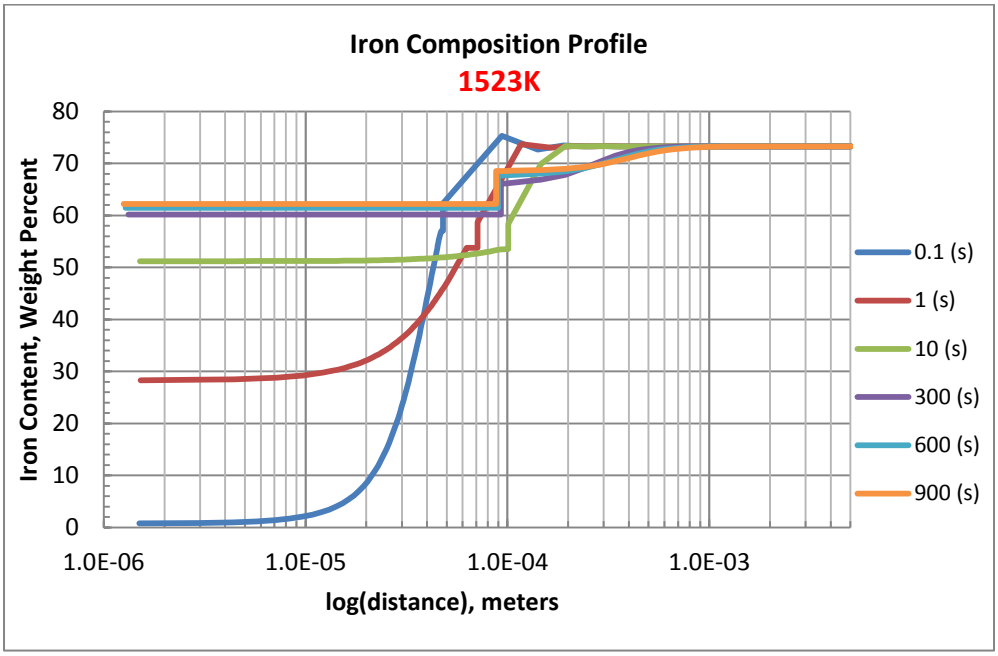

Figure 6.20- The simulated composition profile for iron is shown for various hold times at 1523K.

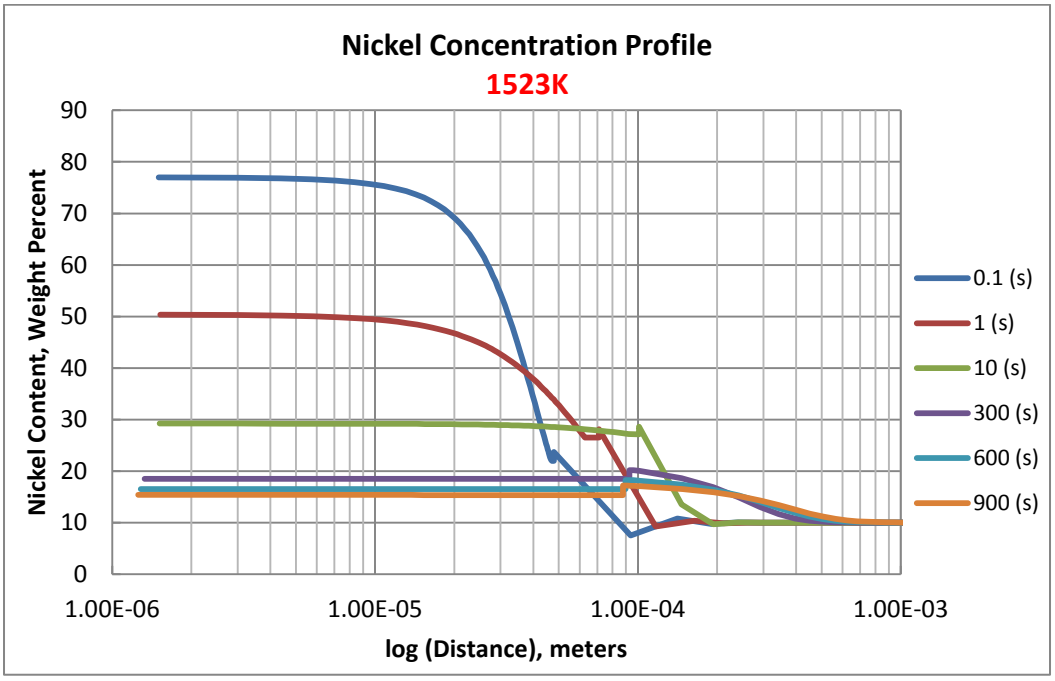

Figure 6.21- The simulated composition profile for nickel is shown for various hold times at 1523K.

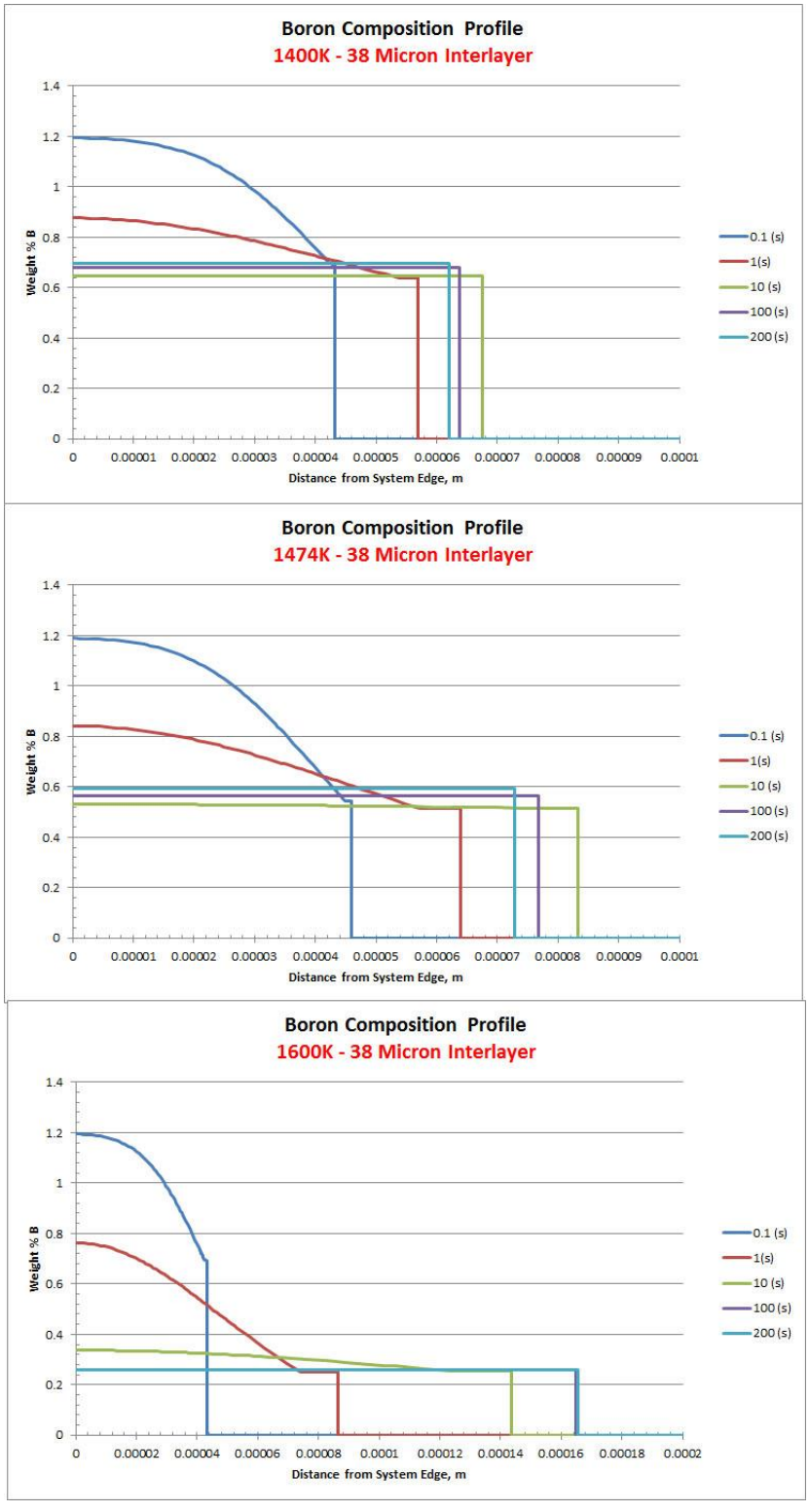

Figure 6.22- The simulated composition profile for boron is shown at 1400, 1474, and 1600 K for various hold times.

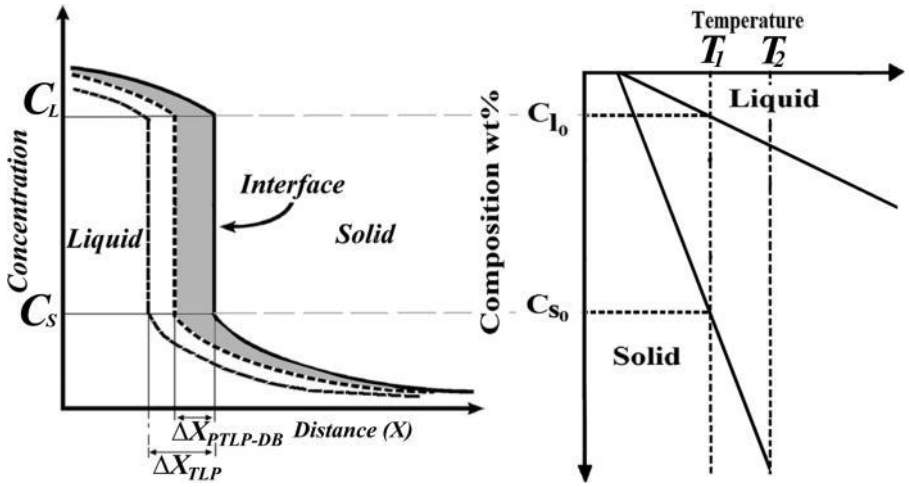

Figure 6.23- The assumption of equilibrium at the interface results in sharp composition profile that is discontinuous at the liquid/solid interface [34].

The expected effects of boron and silicon diffusion can be estimated from equilibrium calculations, as shown in calculated property diagrams at different temperatures (Figures 6.24 through 6.26). When the amounts of the other elements in the system are held constant, the interrelation of boron and silicon as melting point depressants become immediately apparent – as increasing amounts of boron diffuse from the liquid into the substrate, less silicon diffusion is necessary to initiate isothermal solidification. For example, if the initial boron content of 1.23wt% is held constant, approximately 5.4wt% silicon must diffuse from the liquid into the substrate to initiate isothermal solidification; however, if the boron is constant at 0.1wt%, only 3.1wt% of the silicon needs to diffuse. In the absence of boron, the system can be approximated by the Ni-Si binary phase diagram. Similar procedures were performed to study the effect of iron and chromium levels. It was found that the presence of elevated iron and chromium in the liquid, such as during substrate dissolution, has a negligible effect on the isothermal solidification thermodynamics.

The interrelation of boron and silicon in addition to the presence of boride and silicide intermediate phases indicate that binary phase diagrams cannot be reliably used to model the type 316L/MBF-51 system.

Multiple attempts at constructing ternary phase diagrams, specifically the Ni-Si-B system were also attempted and compared with published data [58]. These attempts were unsuccessful; however, as neither nickel nor boron are available in the thermodynamic ternary database (PTERN). The use of elements from the binary databases was attempted, but the published reference diagrams could not be reproduced.

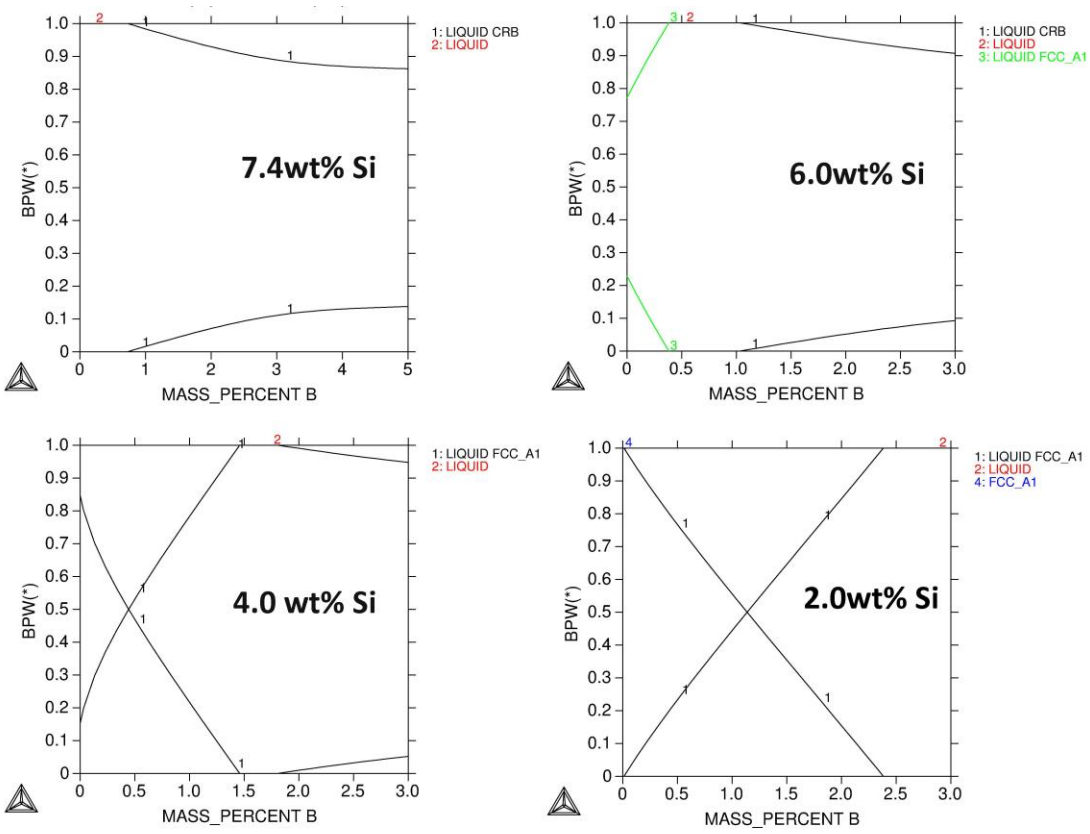

Figure 6.24- The effect of boron concentration on isothermal solidification as a function of silicon content at 1423 K.

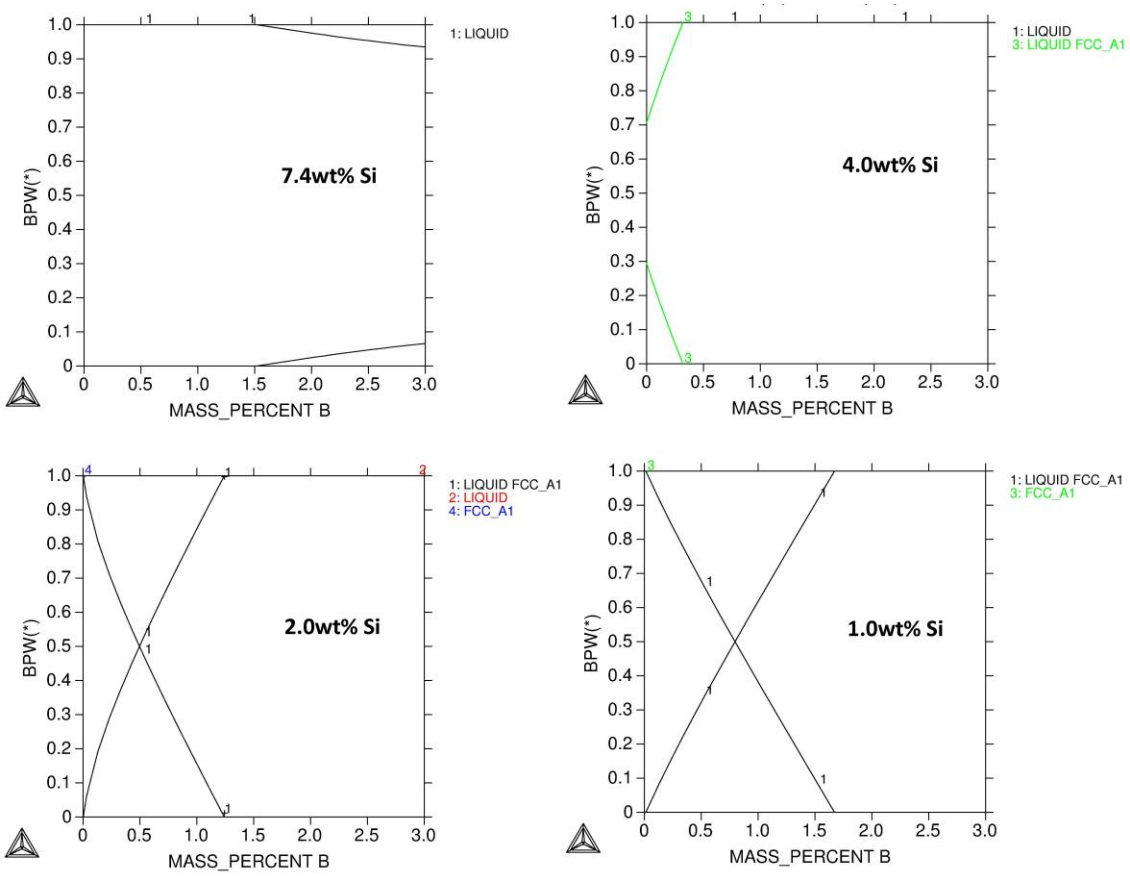

Figure 6.25- The effect of boron concentration on isothermal solidification as a function of silicon content at 1523K.

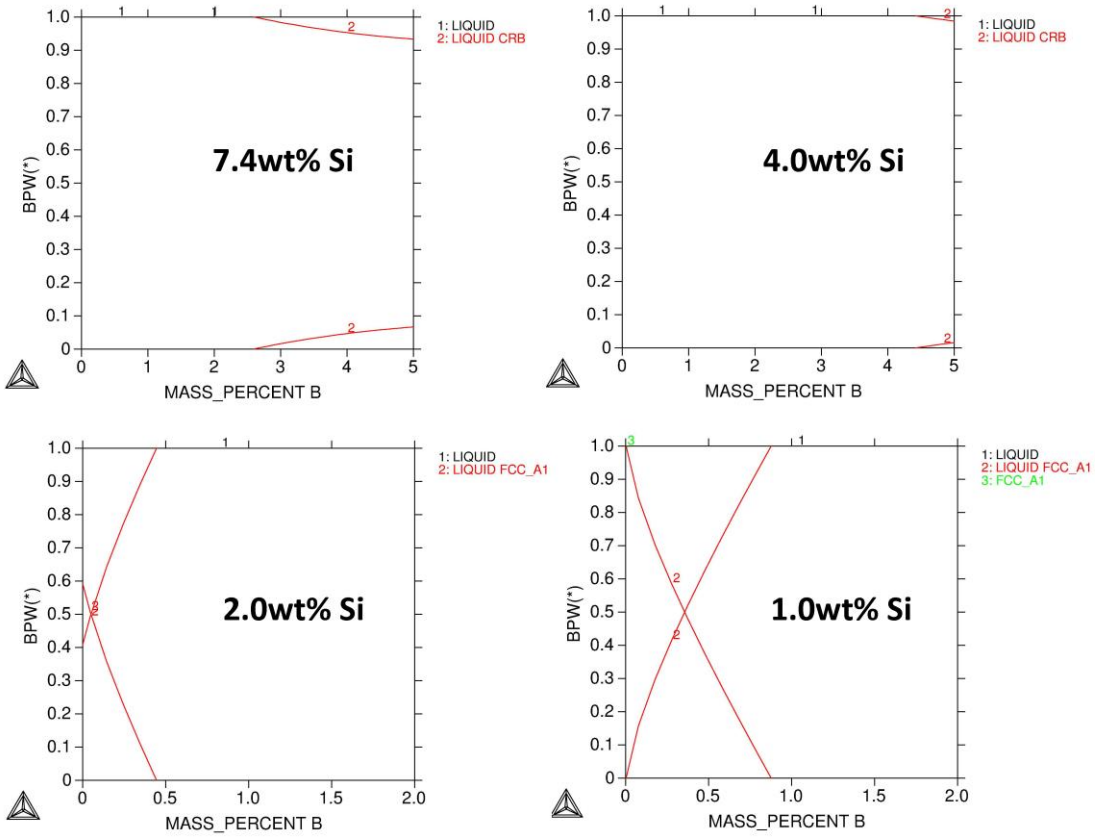

Figure 6.26- The effect of boron concentration on isothermal solidification as a function of silicon content at 1600 K.

7. Comparison of Results

7.1 Position of Interface

Table 7.1 lists the results of the experimental and simulation interface positions for the simulations performed at 1424 K, shown graphically in Figure 7.1.

Table 7.1 – *Comparison of Experimental and Simulation Position of Interface Results at 1424 K*

Time, seconds	Interface Position, meters (microns)		Difference, meters	Relative % Difference
	Experimental	Simulation		
360	2.47E-05 (24.7)	5.65E-05 (56.5)	-3.18E-05	-78.33
3600	2.26E-05 (22.6)	4.00E-05 (40.0)	-1.74E-05	-55.59
18000	1.52E-05 (15.2)	3.28E-05 (32.8)	-1.76E-05	-73.33

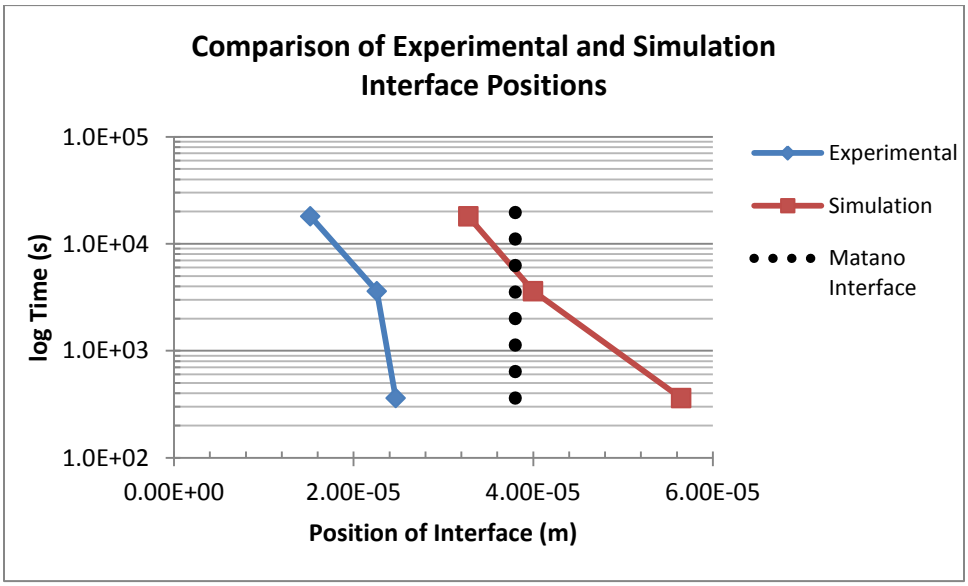

Figure 7.1– The experimental (blue) and simulation (red) interface positions at 1424 K are plotted at 360, 3600, and 18000 seconds.

The results indicate that the experimental interface is already well into the process of liquid layer contraction via isothermal solidification at 360 seconds, while the simulation does not cross back over the Matano interface until approximately 3600 seconds – an order of magnitude "behind" the experimental interface. No data was available to determine the maximum gap width and time of dissolution for the experimental sample; however, the comparisons unambiguously indicate that isothermal solidification occurs significantly faster in the experimental sample than predicted in the simulation. This is presumably due the greater amounts of dissolution (larger gap width) and relatively sluggish isothermal solidification rates in the simulations. The longer simulation times for isothermal solidification may be partly explained by Gale and Butts [22], who inferred that increasing amounts of dissolution during dissolution will cause longer solidification times due to the dependence of isothermal solidification rate on long range diffusion through a solid.

The bulk diffusion coefficient at 1423 K, calculated from isothermal solidification region of the simulated position of interface graph, is 4×10^{-16} m^2/s (Figure 7.2), and is consistent with the experimentally reported value.

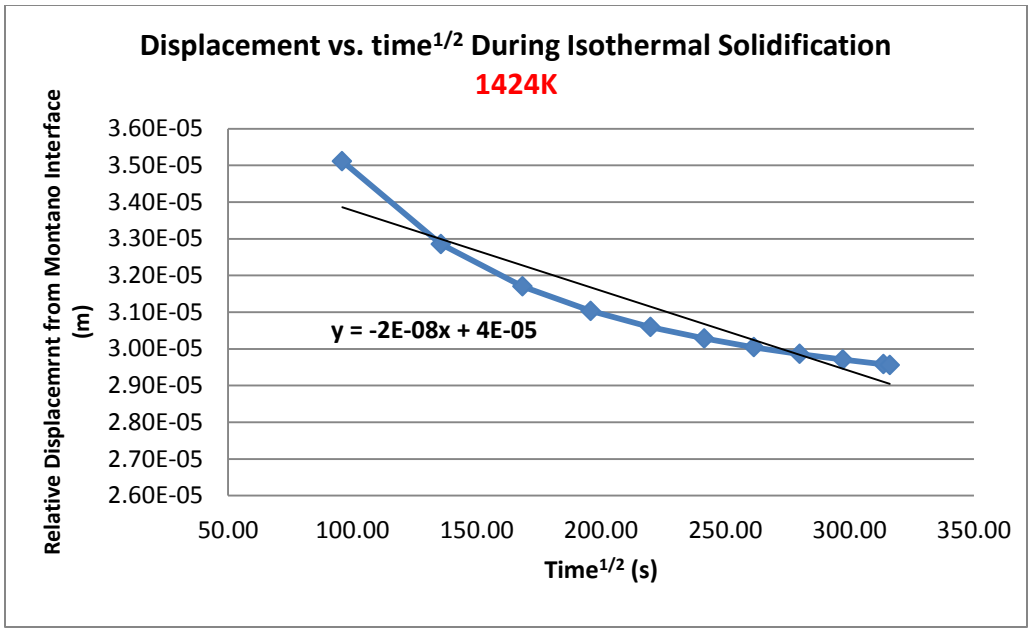

Figure 7.2- The diffusion coefficient for the 1423 K simulation was calculated from the isothermal solidification region of the position of interface curve. The slope of the regression line is the square root of the diffusion coefficient.

7.2 Concentration Profiles

Graphical comparisons of the concentration profiles for the EDS and simulation results are shown in Figures 7.3 through 7.6.

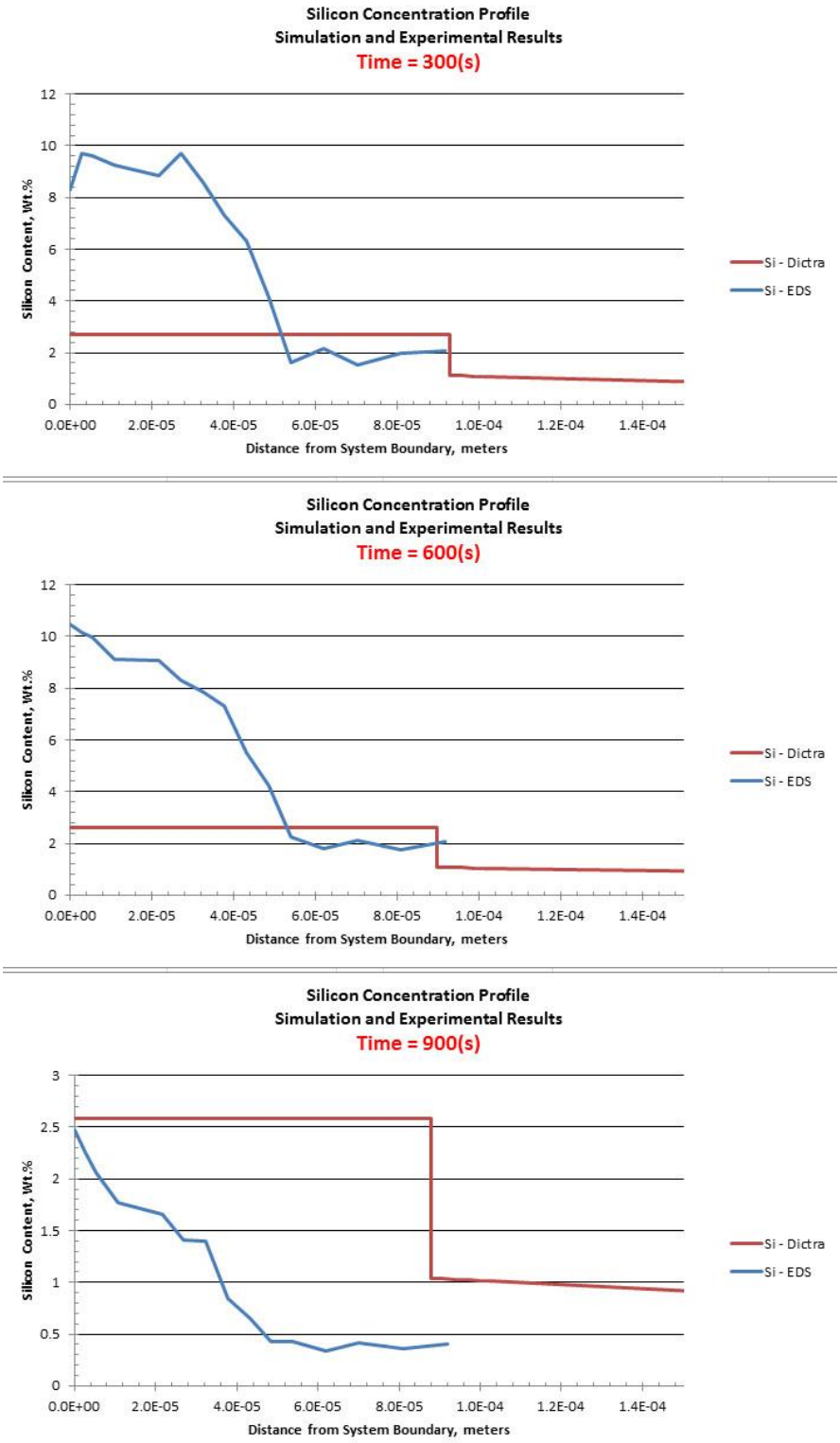

Figure 7.3- Comparison of the silicon concentration profiles from the foil edge (X=0) to 9.02 X 10^{-6} meters deep.

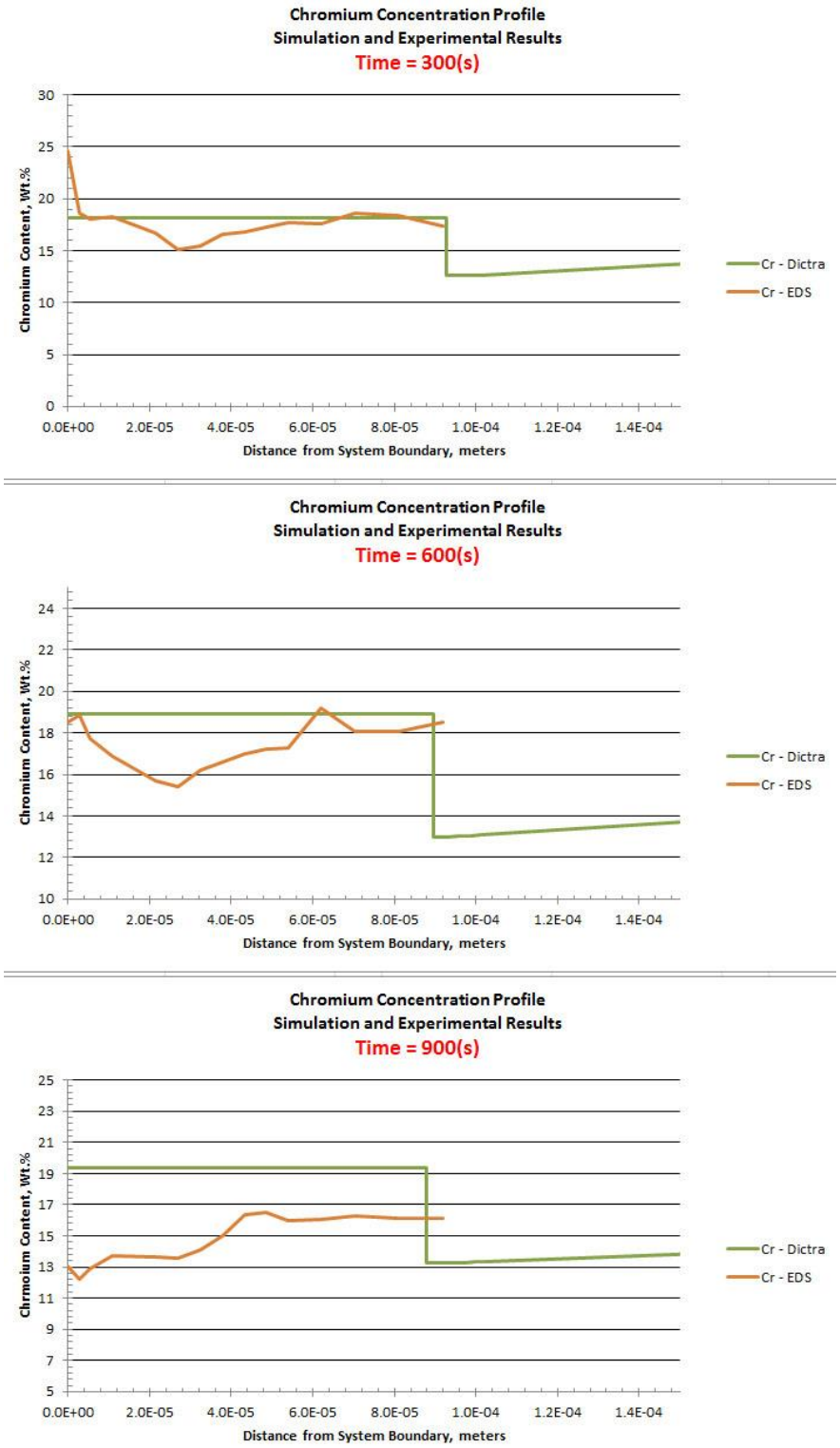

Figure 7.4- Comparison of the chromium concentration profiles from the foil edge (X=0) to 9.02 X 10^{-6} meters deep.

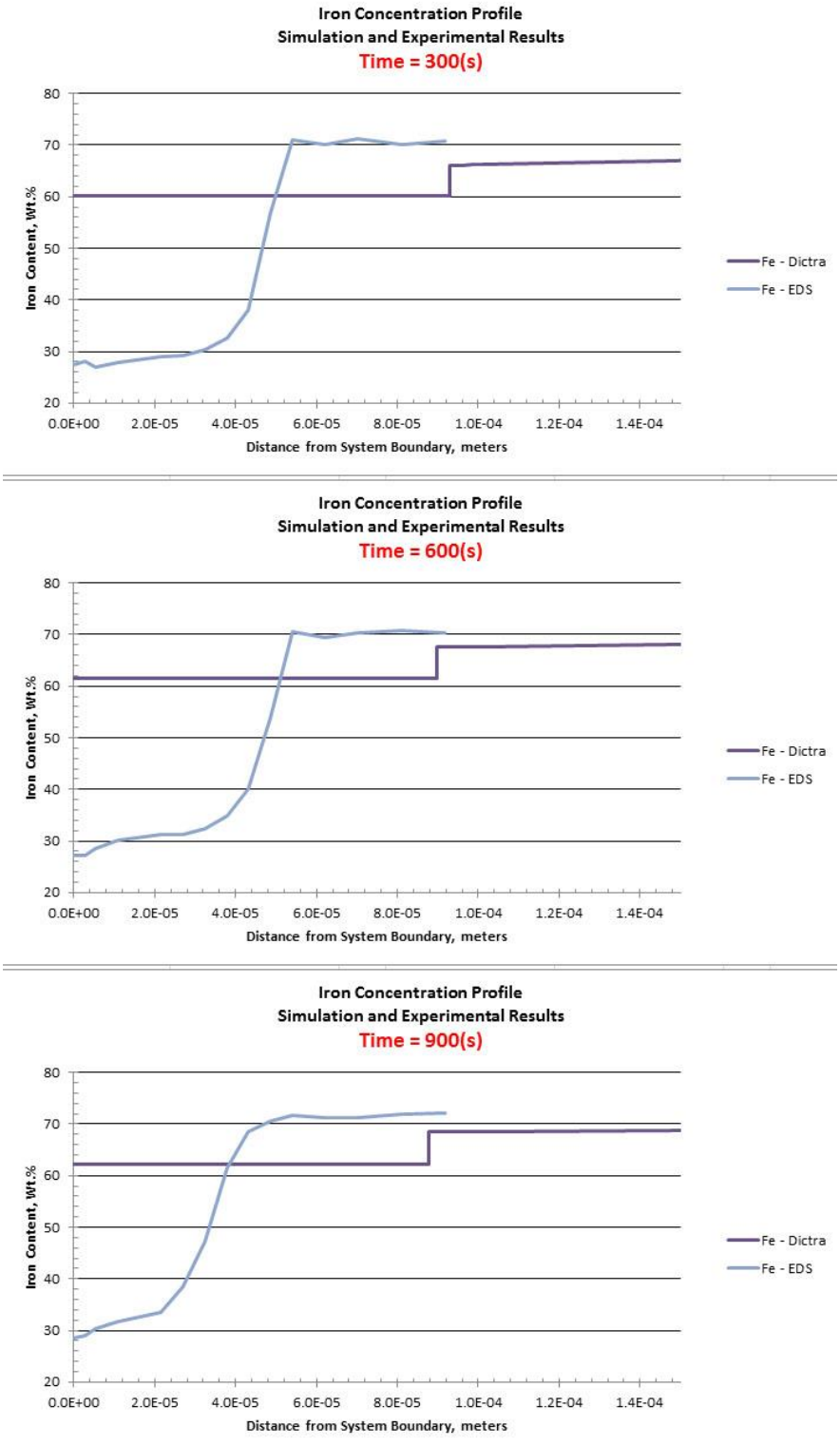

Figure 7.5- Comparison of the iron concentration profiles from the foil edge (X=0) to 9.02 X 10^{-6} meters deep.

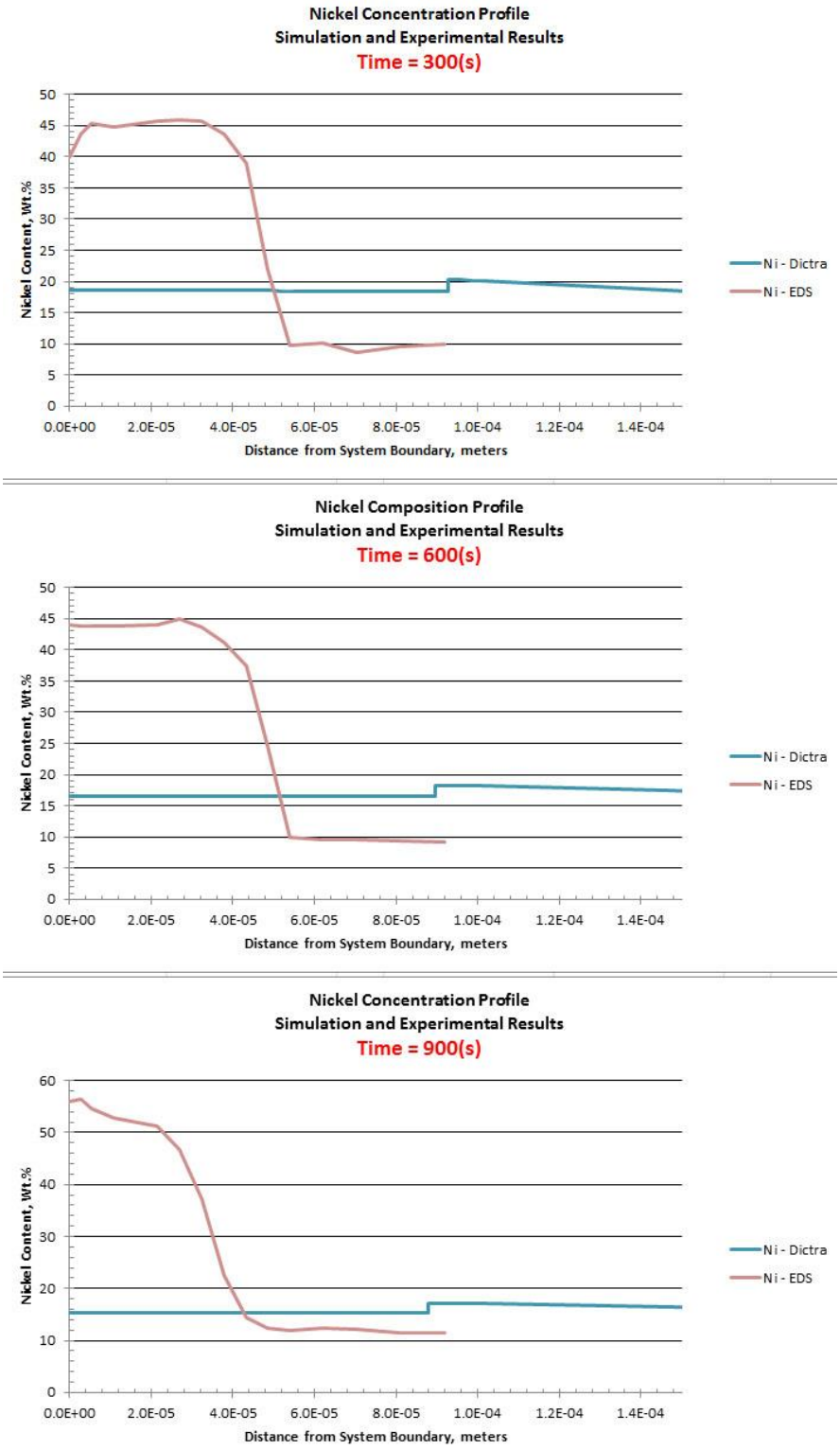

Figure 7.6- Comparison of the nickel concentration profiles from the foil edge (X=0) to 9.02 X 10^{-6} meters deep.

Estimating the final interface positions from the experimental composition profiles and comparing the compositions at the respective interface, regardless of the difference in the interface positions between the simulation and experimental results, allows an approximate comparison of interface compositions, as shown for silicon in Table 7.2

Table 7.2 *– Comparison of Silicon Concentrations at the Solid-Liquid Interface*

Isothermal Hold Time, seconds	**Experimental**		**Simulation**	
	Approximate POI, microns	Wt.% Si at Interface	POI, microns	Wt.% Si at Interface (liquid/fcc)
300	52	2.8	92	2.7/1.2
600	52	2.6	90	2.6/1.2
900	32	1.4	88	2.6/1.0

Table 7.2 shows that the silicon concentrations at the interface are approximately 0.8wt.% and 0.7wt.% lower in the simulations than detected with EDS; respectively. At 900 seconds, the average simulation silicon concentration is 0.4wt% higher than detected by the EDS. Considering the accuracy of element quantification with EDS, these results are in good agreement with one another.

The primary discrepancy in the graphical comparison of concentration profiles is caused by the differences in the simulated and experimental interface positions. Note that direct comparison of the composition profiles exhibit good correspondence if profiles representing shorter simulation times are compared to the 300, 600, and 900 seconds

experimental profiles; e.g. the composition profile after 0.1 second of simulation approximately matches the 300 and 600 (s) profiles of the experiment. As hold time increases; however, the discrepancy between methods becomes smaller.

8. Potential Sources of Error

In the course of this investigation, certain potential errors were observed and should be briefly discussed for consideration in future work.

8.1 Simulations

- One-dimensional modeling and the neglect of grain boundary diffusion are anticipated as a source of error.
- The assumption that local equilibrium exists at the interface complicates comparison because it can only be an approximation and some systems may show deviation from this assumption to an extent that it may not accurately represent kinetics. Also, the assumption of a planar interface may complicate comparisons with experimental data.
- Most of the empirical equations dealing with maximum interlayer width, percent liquid, or liquid composition are developed for binary systems and, therefore are difficult to apply to higher-order systems.
- User errors due to a significant learning curve and lack of explanations for error messages received when attempting to run simulations.
- The phases modeled (liquid and FCC) are likely inadequate to represent the actual system kinetics. The most important shortcoming is the inability to absence of kinetic data for boride phases.

- The lack of elements in the ternary system may also impact how the system is simulated as MBF-51 is a ternary system.

8.2 Experimental

8.2.1 DSC

- The mass of the substrate is significantly higher than the foil, which causes the substrate to act as a heat sink. This reduces the total heat of formation measured by the DSC [33].
- The trend line for percent remaining vs. $\sqrt{t}$ does not intersect the y-axis at unity, which makes the determination of the isothermal solidification time by extension of the trend line to the x-axis suspect.
- Primary solidification occurs via epitaxial growth and will not show up on the exothermic peaks of the DSC.

8.2.2 SEM/EDS

- Due to the normalization of results and inherent shortcoming with detection, the accuracy of EDS measurements are not always as accurate as conventional chemical evaluation methods.

8.2.3 Metallography

- The phase boundaries are difficult to resolve and the interface position is not constant.

8.3 Comparisons

- The accuracy of distance measurements is a significant variable when comparing results; especially working with micron-size length scales.
- Using only the few sets of experimental data needed to solve for the diffusion coefficients and diffusion equations and trying to mimic with a simulation will often lead to difficulties experiments are performed on the same system and conditions, different results will be obtained.
- Difficulties in interpreting others experimental data can present significant difficulties.

9. Conclusions

The purpose of this investigation was to determine if computerized numerical simulation software could be used by a novice to model the thermodynamics and kinetics of TLP bonding. Multiple simulation scenarios were attempted; however, convergence failures present a difficult and time-consuming task for an inexperienced user.

The results of this investigation indicate that given the variables used for the simulations, DICTRA has limited predictive capability for transient liquid phase solidification in the type 316L - MBF-51 system. This is thought to be caused primarily by the lack of kinetic models in DICTA for boride phases.

In the type 316L/MBF-51 system investigated, the diffusion of boron is the primary chemical factor in TLP solidification of this system. Upon solidification due to cooling (i.e. eutectic solidification) the remaining liquid, which can be approximated as an iron-nickel alloy in most cases, boron is rejected due to low solid saturation limits in both nickel and iron. The rejected boron forms an interstitial intermediate compound, which are various boride phases. These boride phases act as boron enriched “sinks” that effectively lower the boron concentration in the adjacent solid and liquid. It is hypothesized that this local reduction of boron in the liquid initiates more isothermal solidification. Therefore, when boride formation is not included in the kinetic model, a

potential contributing factor to isothermal solidification in this system is neglected. To summarize, the exclusion of boride phases in the DICTRA simulations is hypothesized to be a significant source of error in the simulations.

While the numerical simulations are not in full agreement with the expected and experimental results, the model does help develop understanding of solidification in the 316L/MBF-51 system. Also, the simulation can effectively model the dissolution and widening aspects of TLP bonding; stages that evade reliable prediction and characterization by analytical methods and DSC evaluation, respectively. Additionally, the creation and modification of kinetic databases with experimentally derived thermodynamic and mobility data for a given process is also expected to greatly improve the correlation of experimental and simulation results.

While thermodynamic and kinetic simulations have potential to be a very useful tool in aiding the sampling by narrowing down of the potential sample matrix, successful implementation requires experience and skill with the implicit limitations of the models and software. Because novice level troubleshooting aids and error checking tools are lacking in number and even more so in content, a strong background in heterogeneous equilibria, phase theory, and atomic kinetics is also necessary when designing models to reliably simulate real processes.

10. Future Work

Improvement in the definition of accurate simulation parameters for the type 316L / MBF-51 system are a necessary condition before the simulations will closely approximate the actual process. This should include:

- Derivation of kinetic data necessary for modeling of the boride phases. If this is restrictively difficult or time-consuming, indirect methods of representing boride phases, such as other intermediate or intermetallic phases that approximate boride kinetics and are already in the kinetic database, could be used.
- A mobility database that is specifically designed for high nickel alloys may better represent the kinetics of the MBF-51.

After the problem of treating boride kinetics, the following could be done to improve accuracy.

- Add a heating step to study the effects of heating rates.
- Once the model predicts isothermal solidification more regularly, the homogenization stage may be modeled.
- Holding at a lower simulation temperature after the initial braze temperature is achieved.

- Document the effects of varying time steps and grid points for a given simulation.

Finally, a significant amount of researchers have used Thermo-Calc and DICTRA for simulation of TLP bonding and associated processes. Most of the papers have graphs similar to those shown in this investigation; however, none exhaustively detail how the results were obtained – it seems to be assumed that the reader either (1) knows the software so well that relation of methods would be redundant, or (2) the reader only cares that the simulation results match the experimental and cares little *why* it matches the experimental results. This must be remedied as it creates a considerable barrier to replication of results and fundamental understanding of simulation methodology.

11. References

[1] G.H. David M. Jacobson, Principles of Brazing, ASM International, Materials Park, OH, 2005.

[2] W.D. MacDonald, T.W. Eagar, Annual Review of Materials Science, 22 (1992) 23-46.

[3] M.L. Kuntz, Mechanical Engineering, University of Waterloo, Waterloo, Ontario, Canada, 2006, pp. 214.

[4] I.D. Tuah-Poku, M.; Massalski, T.B.;, Metallurgical and Materials Transactions A, 19A (1988) 675-686.

[5] M.A. Arafin, M. Medraj, D.P. Turner, P. Bocher, 3rd International Brazing and Soldering Conference, ASM International, Crowne Plaza Riverwalk Hotel, San Antonio, Texas, USA, 2006.

[6] G.O. Cook, C.D. Sorensen, Journal of Materials Science, 46 (2011) 5305-5323.

[7] E. Lugscheider, K.D. Partz, Welding Journal, (1983) 160-s - 164-s.

[8] E. Lugscheider, T. Schittny, E. Halmoy, Welding Journal, (1989) 9-s - 13-s.

[9] O.A. Ojo, N.L. Richards, M.C. Charturvedi, Science and Technology of Welding and Joining, 9 (2004) 209-220.

[10] R.L. Peaslee, M.J. Lucas, Diffusion Brazing, in: A.W.S.A.C.C.o.B.a. Soldering (Ed.) Brazing Handbook, American Welding Society, Miami, FL, 2007, pp. 341-350.

[11] A. Luo, A, in: M. Li, C. Campbell, K. Thornton, E. Holm, P. Gumbsch (Eds.) 2nd World Congress on Integrated Computational Materials Engineering, TMS, 2013, pp. 7.

[12] y.Z. K. Ikeuchi, h. Kokawa, T.H. North, Metallurgical and Materials Transactions A, (1992).

[13] in: I. Metglas (Ed.), Brochure.

[14] M.A. Arafin, M. Medraj, D.P. Turner, P. Bocher, Materials Chemistry and Physics, 106 (2007) 109-119.

[15] H. Chen, J.M. Gong, S.T. Tu, Science and Technology of Welding and Joining, 14 (2009) 32-41.

[16] M.A. Arafin, M. Medraj, D.P. Turner, P. Bocher, Materials Science and Engineering: A, 447 (2007) 125-133.

[17] J.E. Ramirez, S. Liu, Welding Journal, (1992) 365-s - 375-s.

[18] Y. Zhou, W.F. Gale, T.H. North, International Materials Reviews, 40 (1995) 16.

[19] N. Di Luozzo, M. Fontana, B. Arcondo, Journal of Materials Science, 43 (2008) 4938-4944.

[20] J. Ruiz-Vargas, N. Siredey-Schwaller, N. Gey, P. Bocher, A. Hazotte, Journal of Materials Processing Technology, 213 (2013) 20-29.

[21] D.M. Turriff, S.F. Corbin, M. Kozdras, Acta Materialia, 58 (2010) 1332-1341.

[22] W.F. Gale, D.A. Butts, Science and Technology of Welding and Joining, 9 (2004) 283-300.

[23] C.W. Sinclair, Journal of Phase Equilibria, 20 (1999) 9.

[24] C.W. Sinclair, G.R. Purdy, J.E. Morral, Metallurgical and Materials Transactions A, 31A (2000) 6.

[25] K.W. Moon, W.J. Boettinger, U.R. Kattner, F.S. Biancaniello, C.A. Handwerker, Journal of Electronic Materials, 29 (2000) 24.

[26] W.J. Boettinger, C.E. Coriell, C.E. CAMPBELL, G.B. McFadden, Acta Materialia, 48 (2000) 12.

[27] C.E. Campbell, W.J. Boettinger, Metallurgical and Materials Transactions A, 31A (2000) 13.

[28] M.L. Kuntz, B. Panton, S. Wasiur-Rahman, Y. Zhou, S.F. Corbin, Metallurgical and Materials Transactions A, 44 (2013) 3708-3720.

[29] H. NAKAGAWA, C.H. LEE, T.H. NORTH, Metallurgical and Materials Transactions A, 22A (1991) 13.

[30] G. Izuta, T. Tanabe, K. Suganuma, Soldering & Surface Mount Technology, 19 (2007) 4-11.

[31] S. Mannan, M.P. Clode, Soldering & Surface Mount Technology, 16 (2004) 3.

[32] X.P. Zhang, Y.W. Shi, Scripta Materialia, 50 (2004) 1003 - 1006.

[33] M.L. Kuntz, S.F. Corbin, Y. Zhou, Acta Materialia, 53 (2005) 3071-3082.

[34] S.S. Babu, International Materials Reviews, 54 (2009) 333-367.

[35] F.C. Campbell, Phase Diagrams - Understanding the Basics, ASM, Materials Park, Ohio, 2012.

[36] H.G. Lee, Chemical Thermodynamics For Metals and Materials, 1st ed., Imperial College Press, London, 1999.

[37] M. Hilert, M. Selleby, Thermo-Calc Software, Stockholm, Sweden, 2013, pp. 64.
[38] U.R. Kattner, Journal of Metals, 49 (1997) 14-19.

[39] P. Mason, A. Engstrom, J. Agren, S. Hallstrom, in: D.U. Furrer, S.L. Semiatin (Eds.) ASM Handbook, Volume 22B, Metals Process Simulation, ASM, 2010.

[40] J.-O. Andersson, T. Helander, L. Hdghmd, P. Shi, B. Sundman, Calphad, 26 (2002) 40.

[41] A. Borgenstam, A. Engstrom, L. Hoglund, J. Agren, Journal of Phase Equilibria, 21 (2000) 12.

[42] J. Morral, F. Meisenkothen, Modeling Diffusion in Binary and Multicomponent Alloys, in: D.U. Furrer, S.L. Semiatin (Eds.) ASM Handbook, Volume 22A: Fundamentals of Modeling for Metals Processing, ASM, 2009.

[43] W.J.B. C.E. Campbell, Metallurgical and Materials Transactions A, (2000).

[44] T. C. Illingworth, I.O. Golosnoy, V. Gergely, T.W. Clyne, Journal of Materials Science, (2005) 7.

[45] T.C. Illingworth, I.O. Golosnoy, T.W. Clyne, Materials Science and Engineering: A, 445-446 (2007) 493-500.

[46] X. Yuan, M.B. Kim, C.Y. Kang, Metallurgical and Materials Transactions A, 42 (2010) 1310-1324.

[47] Y. Li, W. Liu, P. He, J. Feng, D.P. Sekulic, Journal of Materials Science, 48 (2013) 5247-5252.

[48] M.L. Kuntz, Y. ZHOU, S.F. CORBIN, Metallurgical and Materials Transactions A, 37A (2006) 12.

[49] W.D. MacDONALD, T.W. EAGAR, Metallurgical and Materials Transactions A, 29A (1998) 11.

[50] S. Acker, in: P. Communication (Ed.), April 2014.

[51] P. Shewmon, Diffusion in Solids, 2 ed., TMS, Warrendale, PA.

[52] R.E. Reed-Hill, Physical Metallurgy Principles, 2 ed., D. Van Nostrand Company, New York, NY, 1973.

[53] S. Wessman, Materials Science, KTH, Stockholm, Sweden, 2013.

[54] Thermo-Calc Software System (Thermodynamic Framework and Data), Foundation of Computational Thermodynamics, Stockholm, Sweden, 2006.

[55] I.B. Laux, Thermo-Calc Users' Meeting, Siemens AG, 2013.

[56] H. Strandlund, KTH, Stockholm, Sweden, 2005.

[57] J.-O. Andersson, J. Ågren, Journal of Applied Physics, 72 (1992) 1350.

[58] T. Tokunaga, N. Kazumasa, H. Ohtani, M. Hasebe, Materials Transactions, 44 (2003) 1651-1654.